

PROCEEDINGS A

royalsocietypublishing.org/journal/rspa

Review

Cite this article: Simpson MJ, McCue SW. 2024 Fisher–KPP-type models of biological invasion: open source computational tools, key concepts and analysis. *Proc. R. Soc. A* **480**: 20240186. <https://doi.org/10.1098/rspa.2024.0186>

Received: 8 March 2024

Accepted: 5 June 2024

Subject Category:

Mathematics

Subject Areas:

applied mathematics, differential equations, mathematical modelling

Keywords:

population biology, diffusion, logistic growth, travelling wave, scientific computation

Author for correspondence:

Matthew J. Simpson

e-mail: matthew.simpson@qut.edu.au

Fisher–KPP-type models of biological invasion: open source computational tools, key concepts and analysis

Matthew J. Simpson and Scott W. McCue

School of Mathematical Sciences, Queensland University of Technology (QUT), Brisbane, Australia

ID MJS, 0000-0001-6254-313X

This review provides open-access computational tools that support a range of mathematical approaches to analyse three related scalar reaction-diffusion models used to study biological invasion. Starting with the classic Fisher–Kolomogorov (Fisher–KPP) model, we illustrate how computational methods can be used to explore time-dependent partial differential equation (PDE) solutions in parallel with phase plane and regular perturbation techniques to explore invading travelling wave solutions moving with dimensionless speed $c \geq 2$. To overcome the lack of a well-defined sharp front in solutions of the Fisher–KPP model, we also review two alternative modelling approaches. The first is the Porous–Fisher model where the linear diffusion term is replaced with a degenerate nonlinear diffusion term. Using phase plane and regular perturbation methods, we explore the distinction between sharp- and smooth-fronted invading travelling waves that move with dimensionless speed $c \geq 1/\sqrt{2}$. The second alternative approach is to reformulate the Fisher–KPP model as a moving boundary problem on $0 < x < L(t)$, leading to the Fisher–Stefan model with sharp-fronted travelling wave solutions arising from a PDE model with a linear diffusion term. Time-dependent PDE solutions and phase plane methods show that travelling wave solutions of the Fisher–Stefan model can describe both biological invasion ($c > 0$) and biological recession ($c < 0$). Open source Julia code to replicate all computational results in this review is available on GitHub; we encourage researchers to use this code directly or to adapt the code as required for more complicated models.

1. Introduction

Population biology can involve examining populations of individuals undergoing some form of migration mechanism together with a birth–death process. The combination of these two individual-level mechanisms can lead to the spatial expansion of that population in the form of moving density fronts. In certain contexts, these moving fronts are referred to as *biological invasion* or waves of *biological colonization*. There are many biological and ecological applications in which biological invasion is important. These range from continental-scale ($25 \times 10^6 \text{ km}^2$) colonization of human populations over thousands of years [1] (figure 1a); forest-scale (10^5 hectare) colonization and growth of tropical rainforests over several decades [2] (figure 1b); and tissue-scale ($1\text{--}2 \text{ mm}^2$) colonization of populations of biological cells over 2 days [3,4] (figure 1c). As these three very disparate motivating examples indicate, the study of biological invasion, and hence the motivation to use mathematical models to explore and interrogate biological invasion, is particularly important in the field of ecology [5–7] and cell biology [8,9]. In the field of cell biology, in particular, invasion fronts of motile and proliferative cells are important in tissue repair [10–14], embryonic development [15–17] and disease progression, such as cancer [18–21].

Continuum models of biological invasion are often extensions of the well-known *Fisher–Kolmogorov* (Fisher–KPP) model that was independently proposed by Fisher [22] as well as Kolmogorov *et al.* [23] in 1937:

$$\frac{\partial \bar{u}}{\partial \bar{t}} = \bar{D} \frac{\partial^2 \bar{u}}{\partial \bar{x}^2} + \bar{\lambda} \bar{u} \left[1 - \frac{\bar{u}}{\bar{K}} \right], \quad (1.1)$$

where $\bar{u} \geq 0$ is a dimensional density [individuals/ L^2] that depends upon dimensional position \bar{x} and time $\bar{t} > 0$. The parameters in the mathematical model are the diffusivity coefficient $\bar{D} > 0$ [L^2/T] that is proportional to the rate at which individuals in the population undergo random, undirected migration, $\bar{\lambda} > 0$ [$/T$] is a growth rate associated with the logistic source term and \bar{K} is the carrying capacity density [individuals/ L^2]. This simple reaction–diffusion model supposes that random movement of individuals in the population corresponds to a macroscopic linear diffusion term, and that the proliferation of individuals is described by a logistic growth term. While this model was first proposed as a theoretical modelling tool in 1937, it was not until 1990 that generalizations of this model were first used to explicitly study wound-healing processes where \bar{u} represents a density of cells that close a wound as a result of random migration and carrying capacity-limited logistic proliferation [10]. While the Fisher–KPP model involves a logistic source term, it is possible to work with a different sigmoid growth function, such as the Richards’, Gompertz or generalized logistic models [24–26].

An important feature of the Fisher–KPP model, and generalizations thereof, is the ability of these time-dependent partial differential equation (PDE) models to support travelling wave solutions. Travelling wave solutions are the long-time limit of a time-dependent solution, $\bar{t} \rightarrow \infty$ [27], where the time-dependent problem is posed on an infinite (or semi-infinite) domain with appropriate boundary conditions. The analysis of travelling wave solutions is a key topic within the applied mathematics literature [28–35]. Within this context, the Fisher–KPP model is often viewed as a prototype model of high interest, especially in terms of senior undergraduate and graduate-level training in mathematical sciences [7–9]. While many methods of analysis have been deployed to interrogate and understand travelling wave solutions of the Fisher–KPP model, computational methods for solving the underlying time-dependent PDE model remain of central importance because travelling wave solutions arise as a long-time limit of the time-dependent solution of the nonlinear PDE model.

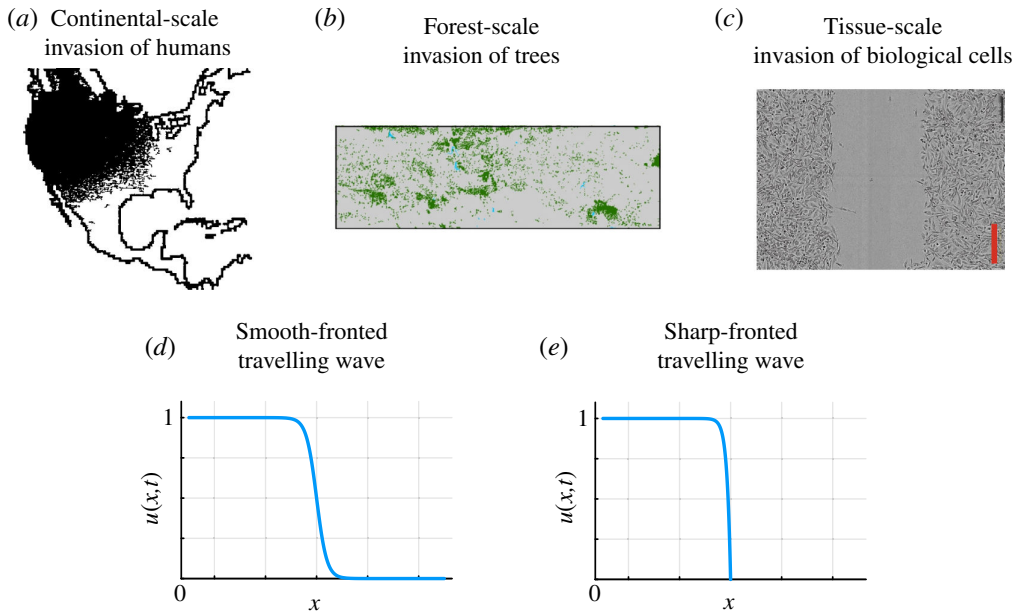


Figure 1. Biological motivation. (a) Continental-scale invasion of populations of humans [1]. (b) Forest-scale invasion of plants and trees during forest recovery in Puerto Rico [2]. (c) Tissue-scale growth and expansion of population of malignant cancer cells [3,4]. All three examples have been modelled using simple extensions of the classic Fisher–KPP model. (d) Schematic travelling wave with a smooth front where $u(x, t) > 0$ on $0 < x < \infty$. (e) Schematic travelling wave with a sharp, well-defined front where $u(x, t) > 0$ for $x < L(t)$, with $x(L(t), t) = 0$.

One well-known feature of travelling wave solutions of the Fisher–KPP model is that the travelling wave solutions are smooth, and do not have compact support as illustrated by the schematic travelling wave profile in figure 1d. This feature is at odds with many biological observations that involve a clear front position [36]. This limitation of the Fisher–KPP model has been dealt with in two different ways. The first approach for introducing a sharp-fronted travelling wave solution is to generalize the linear diffusion term to a degenerate porous-media type nonlinear diffusivity [37–40], giving rise to the *Porous–Fisher* model [9,14,37–44]. A second way of introducing a sharp-fronted travelling wave solution is to re-formulate the Fisher–KPP model, with linear diffusion and logistic growth, as a moving boundary model on $0 < \bar{x} < \bar{L}(\bar{t})$ together with a Stefan-type boundary condition at $\bar{x} = \bar{L}(\bar{t})$ [45,46]. This second type of generalization has been referred to as the *Fisher–Stefan* model of biological invasion [47–52]. As we will show, these three relatively simple scalar reaction–diffusion models give rise to a range of interesting and partly tractable travelling wave solutions that include smooth and sharp-fronted travelling waves as illustrated in figure 1d,e. Furthermore, these models can be used to draw a distinction between *invading* travelling waves where $u(X, t)$ is an increasing function of time at a fixed location X , as well as *receding* travelling waves where $u(X, t)$ is a decreasing function of time at a fixed location X .

The aims of this review are broadly twofold. First, we aim to provide an introduction to the well-known Fisher–KPP (§2) model together with details of the two lesser-known alternatives mentioned above, namely the Porous–Fisher (§3) and Fisher–Stefan (§5) models. As mentioned already, a recurring theme in our discussion will be the ability of each model to describe sharp or smooth moving fronts. While all of these issues have been addressed in the literature, a feature of this review is that we will compare and contrast these three models in a single document that is accessible to graduate students and more experienced researchers alike. Second we present a series of intuitive and easy-to-use open access computational tools to generate time-dependent PDE solutions for the Fisher–KPP, Porous–Fisher and Fisher–Stefan

models. Using computational tools, we relate long-time PDE solutions with associated phase plane analysis and provide open access computational tools to visualize and explore the associated phase planes for travelling wave solutions of each model. We review and derive a range of various perturbation solutions that provide insight into important features of the travelling wave solutions in various asymptotic limits. Finally, we also provide, in the appendix, another set of results for a fourth model that poses the Porous–Fisher model as a moving boundary problem which we call the Porous–Fisher–Stefan model [53]. Again, by providing all of our code written in the open source Julia programming language on [GitHub](#), we aim to provide all researchers with a suite of clear and practical tools to study PDE models for biological invasion that may be used directly or adapted as required.

2. Fisher–KPP model: smooth initial conditions

Starting with the dimensional Fisher–KPP model, [equation \(2.1\)](#), we re-scale density $u = \bar{u}/\bar{K}$, time $t = \bar{\lambda}\bar{t}$ and space $x = \bar{x}\sqrt{\bar{\lambda}/\bar{D}}$ to give a non-dimensional PDE model:

$$\frac{\partial u}{\partial t} = \frac{\partial^2 u}{\partial x^2} + u(1-u), \quad \text{on } 0 < x < \infty, \quad (2.1)$$

whose solution $u(x, t)$ can be re-scaled to correspond to particular choices of dimensional parameters \bar{D} , $\bar{\lambda}$ and \bar{K} to suit different applications.

Relevant boundary conditions are $\partial u / \partial x = 0$ at $x = 0$ and $u \rightarrow 0$ as $x \rightarrow \infty$. For convenience, all time-dependent PDE problems on $0 < x < \infty$ considered in this review focus on initial distributions of u that are concentrated near the origin. To generate numerical solutions of [equation \(2.2\)](#), we work on a truncated domain, $0 < x < L$, where L is chosen to be sufficiently large that we see clear numerical evidence of travelling wave solutions within a sufficiently long, but necessarily finite, duration of time. For this study, we consider the initial condition:

$$u(x, 0) = \begin{cases} u_0 & \text{if } x < b, \\ u_0 e^{-a(x-b)} & \text{if } x > b, \end{cases} \quad (2.2)$$

where $a > 0$ is the exponential decay rate of the initial density, $u_0 > 0$ is the initial maximum population density and $b > 0$ is an initial domain length where $u(x, 0) = u_0$. For computational purposes, we specify no flux boundary conditions at $x = L$, noting that if L is chosen to be sufficiently large the boundary condition at $x = L$ does not play an important role in the time-dependent solution.

To explore the time-dependent solution of [equation \(2.1\)](#), we discretize $0 < x < L$ uniformly with mesh spacing δx so that the location of the i th mesh point is given by $x_i = (i - 1)\delta x$ for $i = 1, 2, 3, \dots, N$. For simplicity, we will write $u(x_i, t)$ as u_i to represent the density at the i th mesh point at time t . Taking a method-of-lines approach [54,55], we approximate the spatial derivative terms in [equation \(2.1\)](#) using a central difference approximation to give a system of semi-discrete coupled nonlinear ordinary differential equations (ODEs):

$$\frac{du_i}{dt} = \begin{cases} \frac{u_{i+1} - u_i}{(\delta x)^2} + u_i(1 - u_i), & \text{if } i = 1, \\ \frac{u_{i-1} - 2u_i + u_{i+1}}{(\delta x)^2} + u_i(1 - u_i), & \text{if } 2 \leq i \leq N - 1, \\ \frac{u_{i-1} - u_i}{(\delta x)^2} + u_i(1 - u_i), & \text{if } i = N. \end{cases} \quad (2.3)$$

Evaluating (2.2) on the finite difference mesh gives the initial condition for the solution of the semi-discrete system (2.3). This system of N ODEs can be efficiently integrated through time to give u_i for $i = 1, 2, 3, \dots, N$ using the DifferentialEquations.jl package in JULIA [56].

Using standard convergence tolerance options, this package implements a range of numerical methods to incorporate automatic time stepping and truncation error control; for this work, we implement a standard 4–5 Runge–Kutta approximation [57]. While all computational results in this review are obtained using explicit methods that use automatic time stepping to control truncation error, other approaches are possible. One alternative is to use operator splitting to combine implicit methods to approximate linear terms with explicit methods to approximate nonlinear terms [58].

Before presenting time-dependent solutions of the Fisher–KPP model, it is worth noting that the only parameters we specify are the initial decay rate a , the length of the domain occupied at maximum initial density b and the initial maximum density u_0 . Preliminary numerical results (not shown) support the well-known result that the long-time travelling wave solutions are independent of u_0 and b , so we focus on the impact of different choices of a for a fixed choice of b and u_0 . Results in figure 2 show four different time-dependent solutions with different values of a ; we will explain how we chose these particular values later. Results in the upper panel of figure 2a correspond to $a = (5 - \sqrt{21})/2$ where we show $u(x, t)$ at $t = 0, 1, 10, 20, 30, 40, 50$ with the arrow showing the direction of increasing time. The initial condition shows the decay of $u(x, 0)$ with position and the short-time solution $u(x, 1)$ shows the impact of the logistic growth term as the density near the origin increases. The subsequent time-dependent solutions at $t = 10, 20, 30, 40, 50$ illustrate that the time-dependent solution approaches a constant shape wave that appears to move with constant speed. To quantify the speed of the wave, we store the solution $u(x, t)$ at $t = 0, 1, 2, \dots, 50$, and at each of the 51 time points, we use linear interpolation to compute the value of X so that $u(X, t) = 1/2$. This computational procedure implicitly defines a function, $X(t)$, describing the time evolution of the position of the wave front. The lower panel of each subfigure in figure 2 gives a scatter plot of $X(t)$ for $t = 0, 1, 2, 3, \dots, 50$ where we see that these points settle to a straight line with positive slope that represents the speed of the wave front during the simulation period. We quantify the speed of the front by taking late-time data, here chosen to be the last five time points (i.e. $t = 46, 47, 48, 49, 50$) and fitting a straight line to these data, and the slope of this straight line gives an estimate of the speed of the front, c .

As suggested by the computational results in figure 2, the long-time travelling wave speed is related to the spatial decay rate of the initial condition, a . It is possible to formalize this putative relationship by supposing we have $u(x, 0) \sim u_0 \exp(-ax)$ as $x \rightarrow \infty$, and considering the motion of the leading edge where $u \ll 1$. Under these conditions, the evolution of the leading edge can be approximated by the solution of a linear PDE [5] by writing $u \sim \hat{u}$, so that:

$$\frac{\partial \hat{u}}{\partial t} = \frac{\partial^2 \hat{u}}{\partial x^2} + \hat{u}, \quad \text{for } \hat{u} \ll 1. \quad (2.4)$$

Assuming the long-time solution takes the form of a constant speed travelling wave with an exponentially decaying front, $\hat{u}(x, t) = \text{const} \times \exp(-a(x - ct))$, where c is the travelling wave speed, we substitute this solution into the linearized PDE to give:

$$c = a + \frac{1}{a}, \quad (2.5)$$

which relates the decay rate of the initial condition a to the long-time travelling wave speed, c . This expression is consistent with the results in figure 2a–c, however, the computational results in figure 2d lead to a slower observed travelling wave speed than indicated by equation (2.5). The reason for the slower than expected travelling wave in figure 2d is that for $a > 1$, a comparison principle limits travelling wave speeds to be $c \leq 2$ [59]. Furthermore, a travelling wave analysis (below) shows that the minimum travelling wave speed possible is $c = 2$. Therefore, for $a > 1$, we have $c = 2$. Together, these conditions give a continuous piecewise relationship:

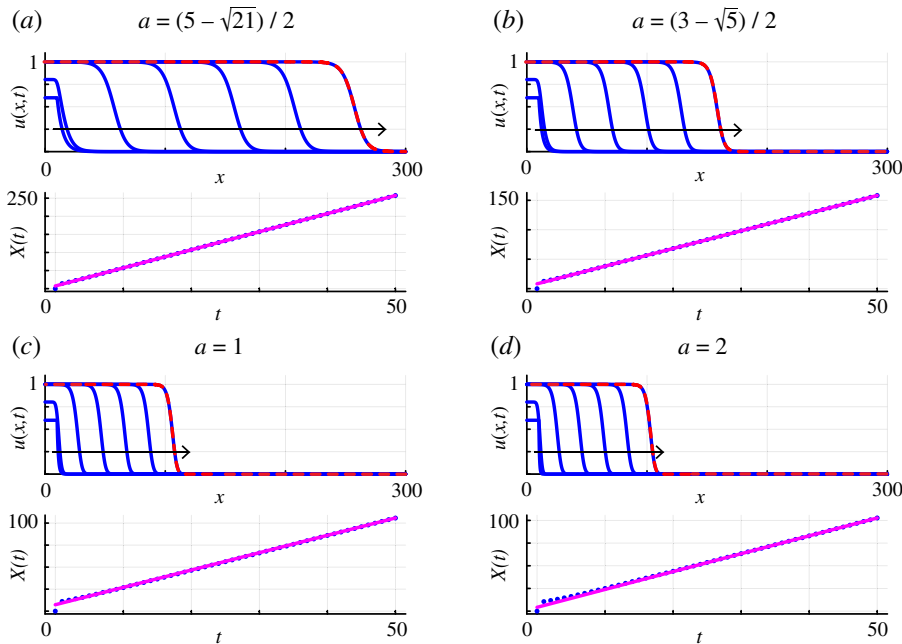


Figure 2. Time-dependent solutions of the Fisher–KPP model illustrate how different initial decay rates of $u(x, 0)$ affect the long-time travelling wave speed c . Four initial conditions, given by (2.2) with $b = 10$ and $u_0 = 0.6$, with varying a are considered: (a) time-dependent PDE solution with $a = (5 - \sqrt{21})/2$ leads to $c = 4.999992423$; (b) time-dependent PDE solution with $a = (3 - \sqrt{5})/2$ leads to $c = 2.999953564$; (c) time-dependent PDE solution with $a = 1$ leads to $c = 1.970531658$; and (d) time-dependent PDE solution with $a = 2$ leads to $c = 1.969077295$. The upper-panel of each subfigure shows $u(x, t)$ (solid blue) at $t = 0, 1, 10, 20, 30, 40, 50$ with the arrow showing the direction of increasing time. Each time-dependent PDE solution at $t = 50$ is superimposed with a dashed red line that corresponds to the shifted $U(z)$ profile obtained in the phase plane. The lower panel shows the time evolution of $X(t)$ where $u(X, t) = 0.5$ for $t = 0, 1, 2, 3, \dots, 50$ (blue dots). Front position data in the lower panel of each subfigure are superimposed with a straight line regression (solid pink) obtained using the last five time points. The slope of the straight line regression gives an estimate of the long-time travelling wave speed, c . Results obtained on $0 \leq x \leq 300$ with $\delta x = 0.1$.

$$c = \begin{cases} a + \frac{1}{a}, & \text{if } a < 1, \\ 2, & \text{if } a > 1, \end{cases} \quad (2.6)$$

where for a sufficiently large, the long-time travelling wave speed is independent of the initial decay rate. This explains the results in figure 2 where we see that slowly decaying initial conditions lead to travelling wave solutions with $c > 2$, whereas rapidly decaying initial conditions with $a \geq 1$ lead to travelling wave solutions that eventually move with the same minimum wave speed $c = 2$. Equation (2.6) is often called the dispersion relationship.

To provide more insight into travelling wave solutions of the Fisher–KPP model, we explore the phase plane by writing the long-time travelling wave solution as $u(x, t) = U(z)$, where $z = x - ct$. It is important to emphasize that working in the travelling wave coordinate implicitly assumes that we are dealing with a long-time solution of the time-dependent PDE where a constant speed and constant shape travelling wave solution has developed. Under these conditions, transforming the time-dependent PDE model into the travelling wave coordinate gives:

$$\frac{d^2U}{dz^2} + c \frac{dU}{dz} + U(1 - U) = 0, \quad \text{on } -\infty < z < \infty, \quad (2.7)$$

with boundary conditions

$$\lim_{z \rightarrow \infty} U(z) = 0, \quad \text{and} \quad \lim_{z \rightarrow -\infty} U(z) = 1. \quad (2.8)$$

Note that equations (2.7)–(2.8) are invariant under translation in z , which means that we may fix the solution by setting $U(0) = 1/2$, for example. Exact, closed-form solutions of this boundary value problem for $U(z)$ are unknown except for the special case of $c^2 = 25/6$ where (2.7) has the Painlevé property [29,35].

To make progress, we study the solution of equations (2.7)–(2.8) in the (U, V) phase plane, where:

$$\frac{dU}{dz} = V, \quad (2.9)$$

$$\frac{dV}{dz} = -cV - U(1 - U). \quad (2.10)$$

At this point, it is interesting to comment on the differences between studying travelling wave solutions of the Fisher–KPP model using the phase plane as opposed to considering long-time solutions of the time-dependent PDE model. As we pointed out previously, the latter involves specifying details of the initial condition, such as the decay rate a , and then solving the PDE to estimate the long-time travelling wave speed c as an *output* of this computational task. By contrast, working with the phase plane implicitly assumes that we have moved to the long-time limit where a travelling wave solution $U(z)$ is relevant, which involves specifying the travelling wave speed c as an *input* to this separate computational task. This means that we can visualize the phase plane for any value of c that we choose, regardless of whether that value arises as a long-time output of a time-dependent PDE solution. This includes travelling wave solutions that are physically unrealistic, as we will explain and demonstrate later.

The dynamical system governing the phase plane (2.9)–(2.10) has two equilibrium points: $(\bar{U}, \bar{V}) = (0, 0)$ and $(\bar{U}, \bar{V}) = (1, 0)$. Linear stability indicates that $(\bar{U}, \bar{V}) = (1, 0)$ is a saddle point for all values of c . The unstable and stable manifolds near the saddle point tend to straight lines passing through $(\bar{U}, \bar{V}) = (1, 0)$ with slopes given by:

$$m_{\pm} = \frac{-c \pm \sqrt{c^2 + 4}}{2}. \quad (2.11)$$

Linear stability analysis indicates that $(\bar{U}, \bar{V}) = (0, 0)$ is a stable spiral for $c < 2$ and a stable node for $c \geq 2$. As we shall explain, this bifurcation at $c = 2$ shows that all physically realistic travelling wave solutions to the Fisher–KPP model have $c \geq 2$.

With this information, we can now visualize various phase planes and explore the consequences of varying c . Results in figure 3 illustrate key features of the phase planes for $c = 3, 2, 1$, respectively. Trajectories in the phase planes are obtained by solving equations (2.9)–(2.10) numerically using DifferentialEquations.jl in JULIA. The phase plane in figure 3a for $c = 3$ shows the two equilibria and a range of trajectories in blue that are included to provide visual interpretation of the full dynamical system. Each blue trajectory is a valid solution of equations (2.9)–(2.10), but these solutions are not relevant in the sense that they are not related to travelling wave solutions of the Fisher–KPP model since they do not satisfy the boundary conditions (2.8). We also show three yellow trajectories and one red trajectory. These four trajectories enter and leave the equilibrium point at $(1, 0)$ along the stable and unstable manifolds and plotting these four trajectories on the phase plane makes the point that $(1, 0)$ is a saddle point. The red trajectory that leaves $(1, 0)$ along the unstable manifold into the fourth quadrant of the (U, V) phase plane enters the origin to form a heteroclinic orbit. Of all the trajectories plotted in the phase plane, it is only this red heteroclinic orbit that has a physical interpretation in terms of the travelling wave solution since it satisfies the boundary conditions (2.8).

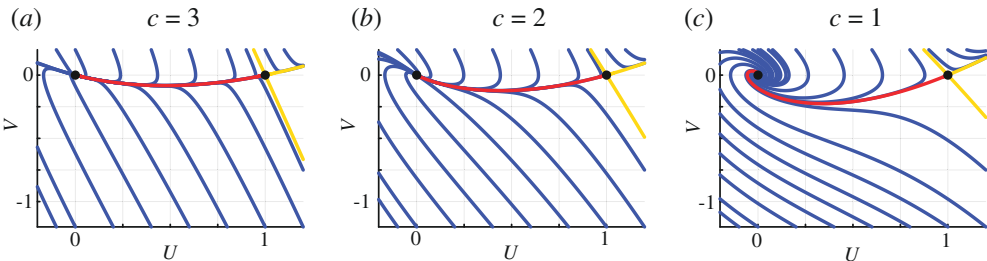


Figure 3. Phase planes for (2.9)–(2.10) with: (a) $c = 3$; (b) $c = 2$; and (c) $c = 1$. Each phase plane show the location of the equilibria (black discs) and several solutions of (2.9)–(2.10). Several solutions (solid blue) are included to provide a complete picture of the dynamical system. Solutions in yellow correspond to those solutions that enter or leave $(1, 0)$ along the stable and unstable manifolds. The heteroclinic orbit leaving $(1, 0)$ along the unstable manifold and entering the fourth quadrant before terminating at the origin is shown in red. Comparing the trajectories near the origin confirm that the origin is a stable node for $c \geq 2$ and a stable spiral for $c < 2$.

We can interpret this red heteroclinic orbit in the phase plane as a parametric curve $(U(z), V(z))$ from which we can plot $U(z)$ and compare the shape of this curve, after applying an appropriate shift in z , with a long-time solution of the time-dependent PDE. The dashed red curve in figure 2b corresponds to $U(z)$ generated in the phase plane, appropriately shifted and superimposed on the late-time PDE solution $u(x, 50)$. Comparing these two curves shows that the shape of the travelling wave solution obtained from the phase plane is visually indistinguishable from the shape of the late-time PDE solution on this scale. Indeed, each upper panel in the four subplots in figure 2 compares the shape of a late-time PDE solution with the shape of $U(z)$, appropriately shifted, obtained from the phase plane for the corresponding value of c .

Results in figure 3b shows a similar phase plane, together with many illustrative blue solution trajectories and the three yellow and one red solution trajectory for $c = 2$. Linear stability indicates that the solution of equations (2.9)–(2.10) locally near the origin bifurcates at $c = 2$ since the origin is a stable node for $c \geq 2$ and a stable spiral for $c < 2$. The borderline case of $c = 2$, shown in figure 3b, indicates that the heteroclinic orbit enters the origin with $U > 0$ as $z \rightarrow \infty$. Taking the shape of the $U(z)$ solution from the phase plane, shifting this profile and superimposing on the late-time PDE solutions in figure 2c,d shows that the shape of the wave obtained from the phase plane is visually indistinguishable from these two late-time PDE solutions that evolved from different initial conditions.

The phase plane in figure 2c for $c = 1$ shows similar features to the two previous phase planes with the exception that we now see the solution of (2.9)–(2.10) spirals into the origin, which implies that $U < 0$ over infinitely many subintervals for $z > 0$. While this trajectory is a valid solution of the dynamical system together with the boundary conditions (2.8), the heteroclinic orbit is not physical in the sense that it does not relate to a late-time solution of the Fisher–KPP model. Therefore, we see that from phase-plane analysis alone, we must have $c \geq 2$. Furthermore, this example makes the point we alluded to earlier that working in the phase plane allows us to specify a value of c regardless of whether that value relates to a long-time output of a time-dependent PDE solution. This observation has often led researchers to discard this phase plane for $c < 2$, however, we will revisit this question later in §5 when we consider the Fisher–Stefan model.

Computational explorations of the time-dependent solutions of the Fisher–KPP model, along with our leading edge and phase plane analysis, confirm that travelling wave solutions of the Fisher–KPP model involve $c \geq 2$. We will now show that it is possible to develop some mathematical insight into the shape of these travelling waves in the limit $c \rightarrow \infty$ by following Canosa [27]. Introducing the change of coordinates $\xi = z/c$ allows us to re-write equation (2.7) as:

$$\frac{1}{c^2} \frac{d^2U}{d\xi^2} + \frac{dU}{d\xi} + U(1 - U) = 0, \quad \text{on } -\infty < z < \infty, \quad (2.12)$$

with boundary conditions

$$\lim_{\xi \rightarrow \infty} U(\xi) = 0, \quad \text{and} \quad \lim_{\xi \rightarrow -\infty} U(\xi) = 1. \quad (2.13)$$

Identifying the small parameter c^{-1} and assuming the solution can be written as a regular perturbation expansion [60]:

$$U(\xi) = U_0(\xi) + \left(\frac{1}{c^2}\right)U_1(\xi) + \mathcal{O}\left(\frac{1}{c^4}\right), \quad (2.14)$$

where we have truncated the expansion so terms of order c^{-4} and smaller are neglected. Substituting this expansion into (2.12) gives:

$$\frac{dU_0}{d\xi} = -U_0(1 - U_0), \quad U_0(0) = \frac{1}{2}, \quad (2.15)$$

$$\frac{dU_1}{d\xi} = -\frac{d^2U_0}{d\xi^2} - U_1(1 - 2U_0), \quad U_1(0) = 0, \quad (2.16)$$

whose solutions, $U_0(\xi)$ and $U_1(\xi)$, can be written in terms of the original independent variable as:

$$U_0(z) = \frac{1}{1 + e^{z/c}}, \quad (2.17)$$

$$U_1(z) = \frac{e^{z/c}}{(1 + e^{z/c})^2} \ln \left[\frac{4e^{z/c}}{(1 + e^{z/c})^2} \right]. \quad (2.18)$$

With these expressions for $U_0(z)$ and $U_1(z)$, we now have a two-term perturbation solution $U(z) = U_0(z) + c^{-2}U_1(z)$ that provides insight into how the shape of the travelling wave solution relates to the travelling wave speed c . Profiles in figure 4a compare the leading-order solution $U_0(z)$, and the two-term perturbation solution $U_0(z) + c^{-2}U_1(z)$ with a late-time solution of the time-dependent PDE for $c = 3$. In this case, we see that the leading-order solution provides a very good approximation of the full travelling wave solution since the differences between the numerical result and the perturbation solution are barely evident at this scale. Further, we see that the two-term perturbation solution is visually indistinguishable from the numerical solution at this scale. Profiles in figure 4b are for the minimum travelling wave speed, $c = 2$, where again we see that the two-term perturbation solution accurately matches the numerical result. The fact that the perturbation solution performs very well for the minimum travelling wave speed illustrates how useful perturbation solutions can be as we are unable to obtain closed form exact solutions for arbitrary values of c , yet these approximate solutions valid in the limit that $c \rightarrow \infty$ turn out to be relatively accurate for just $c = 2$.

More generally, our perturbation solution provides insight into the relationship between the shape of the travelling wave solution and the speed of the wave, c . For example, evaluating the $\mathcal{O}(1)$ perturbation solution at $z = 0$ gives:

$$\frac{dU}{dz} = -\frac{1}{4c} + \mathcal{O}\left(\frac{1}{c^2}\right), \quad (2.19)$$

indicating that the faster the travelling wave speed, the flatter the shape of the wave since we have $dU/dz \rightarrow 0^-$ as $c \rightarrow \infty$ [9].

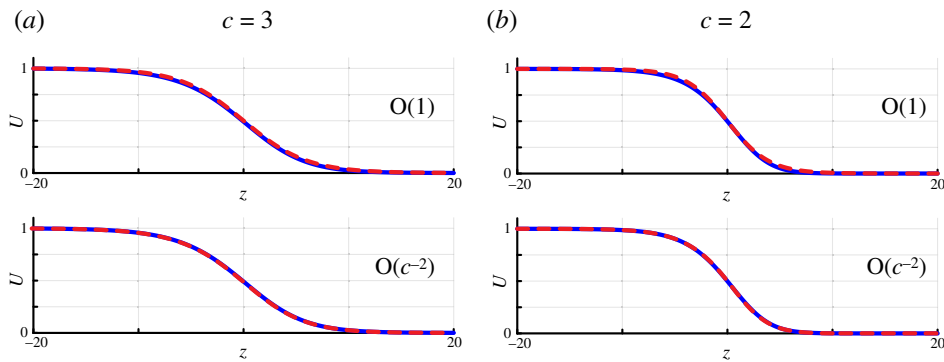


Figure 4. Approximate travelling wave shape given by $c \rightarrow \infty$ asymptotic expressions for: (a) $c = 3$ and (b) $c = 2$. All approximate solutions are compared with the shape of the travelling wave obtained by taking a late-time PDE solution from figure 2b-d, translated so that $U(0) = 1/2$ (solid blue). The upper panels compare the full numerical solution with the $\mathcal{O}(1)$ perturbation approximation $U_0(z)$ and the lower panels compare the full numerical solution with the $O(c^{-2})$ perturbation approximation $U_0(z) + c^{-2}U_1(z)$.

3. Porous–Fisher model: smooth initial conditions

As explained in §2, one of the limitations of travelling wave solutions of the Fisher–KPP model is that they are smooth with $u > 0$ for all $x > 0$, which means that it is difficult to unambiguously identify the precise position of the leading edge of the moving front. This is a challenge because experimental observations often lead to clearly defined sharp fronts that are incompatible with this feature of the Fisher–KPP model [11,12,40]. As such, considerable effort has been spent in developing and understanding alternative reaction–diffusion models that lead to travelling wave solutions with compact support so that these solutions can be used to clearly identify the position of the moving front. The most common approach is to work with the Porous–Fisher model, which can be written in non-dimensional form as:

$$\frac{\partial u}{\partial t} = \frac{\partial}{\partial x} \left[u \frac{\partial u}{\partial x} \right] + u(1-u), \quad \text{on } 0 < x < \infty, \quad (3.1)$$

with $\partial u / \partial x = 0$ at $x = 0$ and $u \rightarrow 0$ as $x \rightarrow \infty$. The key difference is that the linear diffusion flux in the Fisher–KPP model $\mathcal{J} = -\partial u / \partial x$ is replaced with a degenerate nonlinear diffusive flux $\mathcal{J} = -u \partial u / \partial x$ so that \mathcal{J} vanishes when $u = 0$ [37,39]. For numerical purposes, we will replace the far-field condition with $\partial u / \partial x = 0$ at $x = L$, where the value of L is chosen to be sufficiently large so that this does not affect our numerical solution. We will consider the same initial condition as for the Fisher–KPP model, namely (2.2). To explore time-dependent solutions of the Porous–Fisher model, we discretize (3.1) on the same equally spaced finite difference mesh to give:

$$\frac{du_i}{dt} = \begin{cases} \frac{(u_{i+1} + u_i)(u_{i+1} - u_i)}{2(\delta x)^2} + u_i(1 - u_i), & \text{if } i = 1, \\ \frac{(u_{i+1} + u_i)(u_{i+1} - u_i) - (u_{i-1} + u_i)(u_i - u_{i-1})}{2(\delta x)^2} + u_i(1 - u_i), & \text{if } 2 \leq i \leq N-1, \\ \frac{(u_{i-1} + u_i)(u_{i-1} - u_i)}{2(\delta x)^2} + u_i(1 - u_i), & \text{if } i = N, \end{cases} \quad (3.2)$$

which can be integrated through time using the same JULIA package as for the Fisher–KPP model. The inputs into these time-dependent PDE solutions are the parameters governing the initial condition u_0 , a and b ; long-time PDE solutions can be used to estimate the travelling wave

speed, c . Again, as for the Fisher–KPP model, preliminary explorations (not shown) indicate that c depends upon a , but is independent of u_0 and b .

Results in figure 5 illustrate time-dependent solutions of the Porous–Fisher model with the initial condition given by (2.2) with $a = 1/5, 1/3, 1, 2$. In each case, we see the eventual formation of a constant speed, constant shape travelling wave. Using the same approach as for the Fisher–KPP model, we trace the evolution of $X(t)$, where $u(X, t) = 0.5$, to generate a time series of $X(t)$ data that eventually falls on a straight line with a positive slope. Fitting a straight line regression model to the last five points in this time series gives us an estimate of c . Details of the $X(t)$ data and the straight line regression plot are not shown here as they look almost identical to those shown in figure 2 for the Fisher–KPP model. More information can be obtained by exploring the time-dependent PDE codes available on GitHub.

An important point illustrated by the time-dependent PDE solutions in figure 5 is that solutions with sufficiently slow initial decay rates lead to fast, smooth-fronted travelling wave solutions that qualitatively resemble travelling wave solutions to the Fisher–KPP model in figure 2. Later in this section, we will provide a mathematical explanation of this observation. On the other hand, highlighted in figure 5d is that the smooth initial condition with a sufficiently fast exponential decay appears to evolve into a sharp-fronted travelling wave with a well-defined front position. This is a very different outcome to the Fisher–KPP case and may be interpreted as a favourable feature in terms of mathematical modelling. We will investigate the sharp-fronted solution later, when we explore these travelling wave solutions in the phase plane, and then provide a more detailed explanation of these results in §4.

From a numerical point of view, it is worth noting that results in figures 2 and 3 are obtained on the same domain, $0 \leq x \leq 300$, but we have used a much finer discretization to explore time-dependent solutions of the Porous–Fisher model. Our explorations (not shown) indicate that smooth-fronted solutions of the Porous–Fisher model and the Fisher–KPP model can be obtained using a relatively coarse discretization (e.g. $\delta x = 0.1$) leading to grid-independent results when plotted on this scale. The situation is different, however, with the apparent sharp-fronted solution of the Porous–Fisher model in figure 3d where we require a much finer numerical discretization to accurately resolve the shape of the leading edge of the travelling wave, and to provide an accurate estimate of c . Therefore, unlike the Fisher–KPP model where we find that it is possible to make an appropriate choice of δx so that the numerical algorithm performs reasonably well for a range of a values, much greater care needs to be exercised when solving the Porous–Fisher model numerically because the possibility of sharp-fronted solutions requires much finer resolution. For simplicity, all results in figure 5 are generated with a much finer mesh resolution than the results in figure 2 for the Fisher–KPP model. We encourage the reader to explore the impact of choosing different values of δx using the code provided as it is straightforward to show that smooth travelling wave solutions of the Porous–Fisher model can be very accurate with a much coarser mesh.

Just as we did for the smooth-fronted travelling wave solutions of the Fisher–KPP model, it is possible to relate the long-time travelling wave speed c to the decay rate of the initial condition for smooth-fronted travelling wave solutions of the Porous–Fisher model. Supposing, we have $u(x, 0) \sim u_0 \exp(-ax)$ as $x \rightarrow \infty$ for $a > 0$, we can examine the motion of the leading edge by writing $u \sim \hat{u}$ so that:

$$\frac{\partial \hat{u}}{\partial t} = \hat{u}, \quad \text{for } \hat{u} \ll 1. \quad (3.3)$$

If the travelling wave solution of (3.1) takes the form $\hat{u}(x, t) = \text{const} \times \exp(-a(x - ct))$, substituting this solution into the linearized PDE (3.3) gives the dispersion relationship for the Porous–Fisher model:

$$c = \frac{1}{a}, \quad (3.4)$$

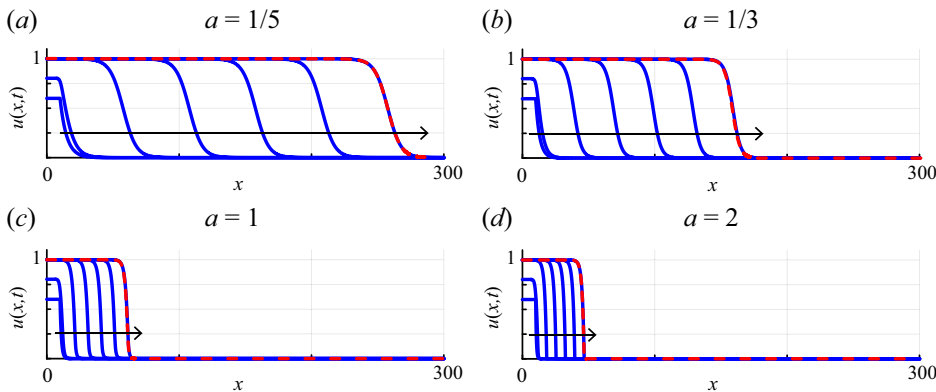


Figure 5. Time-dependent solutions of the Porous–Fisher model illustrate how different initial decay rates of $u(x, 0)$ affect the long-time travelling wave speed c . Four initial conditions, given by equation (2.2) with $u_0 = 0.6$ and $b = 10$, with varying α are considered: (a) time-dependent PDE solution with $\alpha = 1/5$ leads to $c = 5.000000000$; (b) time-dependent PDE solution with $\alpha = 1/3$ leads to $c = 3.000000000$; (c) time-dependent PDE solution with $\alpha = 1$ leads to $c = 0.999999999$; and (d) time-dependent PDE solution with $\alpha = 2$ leads to $c = 0.704887285$. Each time-dependent PDE solution at $t = 50$ is superimposed with a dashed red line that corresponds to the shifted $U(z)$ profile obtained in the phase plane. Results obtained on $0 \leq x \leq 300$ with $\delta x = 0.02$.

which is consistent with the smooth-fronted travelling wave solutions presented in figure 5a–c.

Unlike the Fisher–KPP model, the minimum travelling wave speed for travelling wave solutions of the Porous–Fisher model cannot be determined solely by examining the dispersion relationship and we now turn to the phase plane by writing the long-time travelling wave solution as $u(x, t) = U(z)$, where $z = x - ct$. Transforming the time-dependent PDE model into the travelling-wave coordinate gives:

$$\frac{d}{dz} \left[U \frac{dU}{dz} \right] + c \frac{dU}{dz} + U(1 - U) = 0, \quad \text{on } -\infty < z < \infty, \quad (3.5)$$

with boundary conditions

$$\lim_{z \rightarrow \infty} U(z) = 0, \quad \text{and} \quad \lim_{z \rightarrow -\infty} U(z) = 1. \quad (3.6)$$

As for travelling wave solutions of the Fisher–KPP model, it is not obvious how to solve (3.5) for arbitrary values of c , so we study the solution of this boundary value problem in the (U, V) phase plane where we have [9]:

$$\frac{dU}{dz} = V, \quad (3.7)$$

$$U \frac{dV}{dz} = -cV - U(1 - U) - V^2. \quad (3.8)$$

This dynamical system is singular when $U = 0$, and the singularity can be removed by introducing a transformed independent variable that we write implicitly as [9]:

$$\frac{d}{d\xi} = U \frac{d}{dz}, \quad (3.9)$$

which gives a de-singularized system:

$$\frac{dU}{d\xi} = UV, \quad (3.10)$$

$$\frac{dV}{d\xi} = -cV - U(1 - U) - V^2. \quad (3.11)$$

This de-singularized phase plane has three equilibria: $(\bar{U}, \bar{V}) = (0, 0)$, $(\bar{U}, \bar{V}) = (1, 0)$ and $(\bar{U}, \bar{V}) = (0, -c)$. Linear stability analysis indicates that both $(\bar{U}, \bar{V}) = (1, 0)$ and $(\bar{U}, \bar{V}) = (0, -c)$ are saddle points for all values of c , while the origin is a stable nonlinear node. Similar to the Fisher–KPP model, smooth travelling waves are associated with a heteroclinic orbit between $(1, 0)$ and $(0, 0)$, but we now have the possibility of a sharp-fronted heteroclinic orbit between $(1, 0)$ and $(0, -c)$. In this case, the heteroclinic orbit terminates at $(U, V) = (0, -c)$ meaning that the contact point, where $U = 0$, has a finite negative slope for $c > 0$.

Computationally generated phase planes with various trajectories highlighted are given in figure 6 for key choices of $c = 1, 1/\sqrt{2}, 1/2$. The phase plane in figure 6a for $c = 1$ shows a range of blue trajectories obtained by solving equations (3.10)–(3.11) numerically using codes provided on GitHub. These blue trajectories provide a visual picture of the phase plane within the vicinity of the three equilibrium points. The phase plane also includes seven yellow trajectories that either enter or leave $(0, -c)$ and $(1, 0)$ along the associated unstable and stable manifolds of these saddle node points. Finally, in red, we show the heteroclinic orbit leaving $(1, 0)$ along the unstable manifold into the fourth quadrant of the (U, V) phase plane, eventually entering the origin. This heteroclinic orbit corresponds to the smooth travelling wave solution in figure 5c.

Exploring various phase planes by gradually reducing $c < 1$ indicates that smooth travelling wave solutions, corresponding to a heteroclinic orbit between $(1, 0)$ and $(0, 0)$, persist until we reach some critical value of c where, as the equilibrium point at $(0, -c)$ moves up the V -axis, it becomes possible to have a straight line heteroclinic orbit between $(1, 0)$ and $(0, -c)$, as illustrated in figure 6b. The straight line heteroclinic orbit, $V = -c(1 - U)$, can be substituted into (3.10)–(3.11) to show that the corresponding special travelling wave speed is $c = 1/\sqrt{2}$ [9]. This orbit corresponds to a sharp-fronted travelling wave solution like the results we obtained numerically in figure 5d. Since we now have a mathematical expression for the straight line heteroclinic orbit in the phase plane, we can give a closed-form expression for this special sharp-fronted solution:

$$U(z) = \begin{cases} 1 - e^{z/\sqrt{2}}, & \text{if } z \leq 0, \\ 0, & \text{if } z > 0, \end{cases} \quad (3.12)$$

where this solution has been arbitrarily shifted so the position of the front is $z = 0$. This solution is significant because, unlike the Fisher–KPP model, the Porous–Fisher model leads to travelling wave solutions with a natural front position meaning that this feature can be used to match with experimental observations more easily than working with a smooth-fronted travelling wave solution [14]. To complete the picture, figure 6c shows a phase plane and associated trajectories for $c = 1/2 < 1/\sqrt{2}$ where we now see that there is no longer any possibility of a heteroclinic orbit, indicating that $c = 1/\sqrt{2}$ is the minimum travelling wave speed for the Porous–Fisher model.

For smooth-fronted travelling wave solutions with $c > 1/\sqrt{2}$, we can numerically integrate (3.10)–(3.11) to give numerical estimates of the trajectory in the (U, V) phase plane. This trajectory can be interpreted as a parameterized curve with parameter ζ . Our numerical algorithms on GitHub solve for $U(\zeta)$ and $V(\zeta)$, recording values of these quantities at equally spaced intervals of ζ , with spacing $\delta\zeta$. To compare our numerical estimate of $U(\zeta)$ with numerical solutions of the full time-dependent PDE model in figure 5, we use (3.9) to relate ζ and z , noting that:

$$z(\zeta) = \int^{\zeta} U(\zeta') d\zeta', \quad (3.13)$$

can be evaluated numerically to give a relationship between z and ζ . Since we store values of $U(\zeta)$ at equally spaced intervals of ζ , it is straightforward to compute $z(\zeta)$ by applying the trapezoid rule to evaluate the integral in equation (3.13). While other quadrature methods could be implemented, our approach is simple to implement, and leads to estimates of $U(z)$ that,

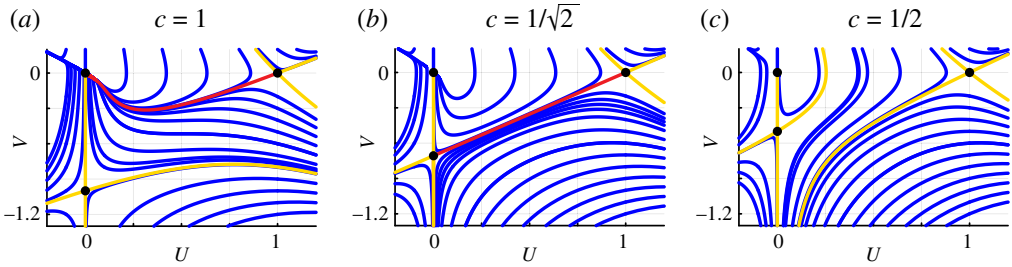


Figure 6. Phase planes for (3.10)–(3.11): (a) $c = 1$; (b) $c = 1/\sqrt{2}$; and (c) $c = 1/2$. Each phase plane show the location of the equilibria (black discs) and several trajectories. Several solutions (solid blue) are included to provide a complete picture of the solution of the dynamical system, solutions in yellow correspond to those solutions that enter or leave $(1, 0)$ and $(0, -c)$ along the stable and unstable manifolds. In (a), the heteroclinic orbit leaving $(1, 0)$ along the unstable manifold and entering the fourth quadrant before terminating at the origin is shown in red, corresponding to a smooth-fronted travelling wave solution. In (b), the straight line heteroclinic orbit leaving $(1, 0)$ along the unstable manifold and entering the fourth quadrant before terminating at $(0, -c)$ is shown in red, corresponding to a sharp-fronted travelling wave solution. In (c), there is no heteroclinic orbit between $(1, 0)$ and either of the other equilibria, indicating that there is no travelling wave solution for this value of c .

after appropriate shifting, compare well with various late-time PDE solutions. Each smooth-fronted time-dependent PDE solution in figure 5a–c includes a dashed red line superimposed on $u(x, 50)$. These dashed red lines correspond to the appropriately shifted $U(z)$ profile obtained from the phase planes; we see that the shape of the travelling wave solution from the time-dependent PDE solution is visually indistinguishable from the profile obtained using the phase plane trajectories. The result in figure 5d for the sharp-fronted travelling wave moving with the minimum travelling wave speed compares the late-time PDE solution with the shifted exact solution (3.12). Again, as for the smooth-fronted travelling wave solutions, here we see that the time-dependent PDE solutions at late time are visually indistinguishable, at least at this scale, from the exact phase plane result.

To conclude this investigation into travelling wave solutions of the Porous–Fisher model evolving from smooth initial conditions, we now develop approximate perturbation solutions to describe the shape of smooth-fronted travelling wave solutions in the limit $c \rightarrow \infty$. Introducing the change of coordinates, $\xi = z/c$, gives:

$$\frac{1}{c^2} \frac{d}{d\xi} \left[U \frac{dU}{d\xi} \right] + \frac{dU}{d\xi} + U(1-U) = 0, \quad \text{on } -\infty < \xi < \infty, \quad (3.14)$$

with boundary conditions

$$\lim_{\xi \rightarrow \infty} U(\xi) = 0, \quad \text{and} \quad \lim_{\xi \rightarrow -\infty} U(\xi) = 1. \quad (3.15)$$

Treating c^{-1} as a small parameter, we assume that the solution can be written as:

$$U(\xi) = U_0(\xi) + \left(\frac{1}{c^2} \right) U_1(\xi) + \mathcal{O}\left(\frac{1}{c^4} \right). \quad (3.16)$$

Substituting this expansion into (3.14) gives

$$\frac{dU_0}{d\xi} = -U_0(1-U_0), \quad U_0(0) = \frac{1}{2}, \quad (3.17)$$

$$\frac{dU_1}{d\xi} = -\frac{d}{d\xi} \left[U_0 \frac{dU_0}{d\xi} \right] - U_1(1-2U_0), \quad U_1(0) = 0, \quad (3.18)$$

whose solutions, $U_0(\xi)$ and $U_1(\xi)$ can be written in terms of the original independent variable as:

$$U_0(z) = \frac{1}{1 + e^{z/c}}, \quad (3.19)$$

$$U_1(z) = \frac{e^{z/c}}{(1 + e^{z/c})^2} \left[\ln 2 - \frac{3}{2} + \frac{3 + (1 + e^{z/c})(z/c - \ln(1 + e^{z/c}))}{1 + e^{z/c}} \right]. \quad (3.20)$$

These expressions give a two-term perturbation solution $U(z) = U_0(z) + c^{-2}U_1(z)$, which provides insight into how the shape of the travelling wave solution relates to c , as we will now explore.

Profiles in figure 7a compare the leading-order solution $U_0(z)$, and the two-term perturbation solution $U_0(z) + c^{-2}U_1(z)$ with a late-time solution of the time-dependent PDE for $c = 3$. As for the Fisher–KPP model, we see that the leading-order solution provides a good approximation of the numerical solution of the full problem. It is useful to recall that travelling wave solutions of the Fisher–KPP model are restricted to $c \geq 2$ and in figure 4b, we saw that a large c asymptotic approximation performed well, even for $c = 2$. With the Porous–Fisher model, we have smooth travelling wave solutions for $c > 1/\sqrt{2}$, which means we can explore the accuracy of a large c asymptotic approximation for even smaller values of c than was possible with the Fisher–KPP model. Profiles in figure 7b for $c = 1$ illustrate that the $U_0(z)$ solution is visually distinct from the full time-dependent solution, whereas the two-term solution gives a reasonably accurate approximation of the shape of the wave, which is remarkable given that we have $c = 1$ and the perturbation approximation is valid for $c \rightarrow \infty$.

It is insightful to note that the $U_0(z)$ term in the large c perturbation solution is identical for the Fisher–KPP and Porous–Fisher models. There are several inferences that can be drawn from this observation. First, we have the same qualitative relationship between the shape and speed of the travelling wave, namely the faster the travelling wave the flatter the shape of the travelling wave for sufficiently large c for both models. Second, this indicates that the shape of a fast-moving travelling wave is primarily determined by the source term in the PDE model rather than the flux term because the influence of the diffusive flux term arises as a correction term, whereas the proliferation mechanism controls the leading order features. This is biologically insightful because while both diffusion and a source term are required to form a travelling wave solution, it is the proliferation term that largely controls the shape of the travelling wave [16].

4. Fisher–KPP and Porous–Fisher models: initial conditions with compact support

All time-dependent PDE solutions considered in §§2 and 3 are mathematically convenient since they have $u(x, 0) \sim u_0 \exp(-ax)$ as $x \rightarrow \infty$ for $a > 0$. This means that the initial conditions shown in figures 2 and 5 are smooth with $u(x, 0) > 0$ for all $x > 0$. This form of initial condition allows us derive a dispersion relationship that relates the exponential decay rate a to the long-time travelling wave speed c , and our time-dependent PDE solutions in figures 2 and 5 are consistent with the dispersion relationship in both cases. This approach, however, is not always preferred since real applications of biological invasion are unlikely to involve an initial distribution that decays exponentially with position [1,3]. An alternative approach is to consider an initial condition of the form:

$$u(x, 0) = \begin{cases} u_0, & \text{if } 0 < x < b, \\ 0, & \text{if } x > b, \end{cases} \quad (4.1)$$

which is far more practical because it models some initial region that is occupied at density u_0 , that is adjacent to another region, $x > b$, which is completely vacant with $u = 0$. This is precisely

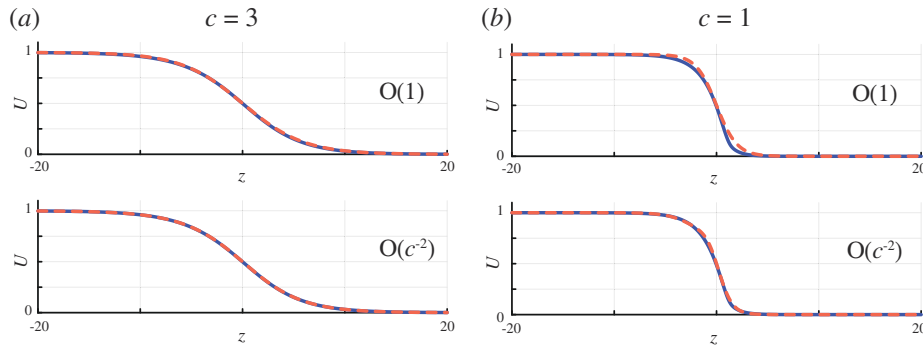


Figure 7. Approximate shape of the smooth-fronted travelling wave solution of the Porous-Fisher model given by $c \rightarrow \infty$ asymptotic expressions for: (a) $c = 3$ and (b) $c = 1$. Each approximate solution is compared with the shape of the travelling wave obtained by taking a late-time PDE solution from figure 5 translated so that $U(0) = 1/2$ (solid blue). The upper panels compare the full numerical solution with the $\mathcal{O}(1)$ perturbation approximation $U_0(z)$ and the lower panels compare the full numerical solution with the $\mathcal{O}(c^{-2})$ perturbation approximation $U_0(z) + c^{-2}U_1(z)$.

the kind of initial condition that is used in the case of applications in cell biology, such as modelling scratch assay experiments [11,12,14,16].

Using our time-dependent PDE algorithms, we can confirm that the long-time shape and speed of the Fisher-KPP and Porous-Fisher solution profiles with the initial condition (4.1) are independent of the choice of u_0 and b (not shown). For example, typical time-dependent solutions are shown in figure 8 where we see that the long-time travelling wave solution of the Fisher-KPP model evolves to the travelling wave solution with the minimum wave speed $c = 2$, while the long-time travelling wave solution of the Porous-Fisher model also evolves to the travelling wave solution with the minimum wave speed with $c = 1/\sqrt{2}$.

It is useful to know that travelling wave solutions evolving from initial conditions with compact support lead to travelling wave solutions with the minimum wave speed. For the Fisher-KPP model, this is consistent with the observation that equation (1.41) can be interpreted as taking $a \rightarrow \infty$ in (2.2), which leads to $c = 2$. The situation for the Porous-Fisher model is more subtle, as we now explain. The results in figure 5 for the Porous-Fisher model involve $u(x, 0) > 0$ for all $x \geq 0$, leading to time-dependent solutions that, despite the apparent sharp front in figure 5d, strictly speaking, all have $u(x, t) > 0$ at all $x \geq 0$ and $t \geq 0$. This is different to the situation in figure 8b, where we have $u(x, 0) > 0$ for $0 < x < b$ and $u(x, 0) = 0$ for $x > b$. In this case, the initial condition with compact support leads to a genuine sharp-fronted time-dependent solution that evolves to the sharp-fronted travelling wave (3.12). Therefore, strictly speaking, the results in figure 8b are the only initial conditions considered so far where there is a clear front position, and the time-dependent solution in figure 8b is the only time-dependent PDE solution where the clear front position persists for $t > 0$. The case in figure 5d where $u(x, 0) > 0$ at all $x \geq 0$ is very interesting because we do not expect to have a time-dependent solution with compact support; we do, however, see the formation of an apparently sharp-fronted travelling wave form at late time, and this travelling wave has the same speed and shape as the minimum speed sharp-front solution (3.12). This observation turns out to be a computational artefact arising because of finite precision arithmetic where the far-field values of the initial condition, $u(x, 0) \sim u_0 \exp(-ax)$, are eventually truncated to zero for sufficiently large values of x , thereby effectively turning the smooth initial condition into one with compact support.

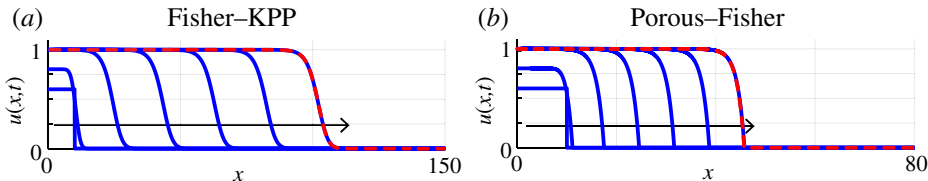


Figure 8. Time-dependent solutions of the Fisher–KPP and Porous–Fisher models evolving from initial conditions with compact support, (4.1) with $u_0 = 0.6$ and $b = 10$. (a) Solutions of the Fisher–KPP model computed on $0 \leq x \leq 150$ with $\delta x = 0.1$ leading to smooth-fronted solutions with $c = 1.969520519$. (b) Solutions of the Porous–Fisher model computed on $0 \leq x \leq 80$ with $\delta x = 0.01$ leading to sharp-fronted solutions with $c = 0.706887186$. Each plot shows $u(x, t)$ at $t = 0, 1, 10, 20, 30, 40, 50$ with the arrow showing the direction of increasing time, and the solution at $u(x, 50)$ is superimposed with a red dashed line corresponding to the shifted $U(z)$ profile obtained in the phase plane.

5. Fisher–Stefan model

The second approach to model travelling wave solutions with a well-defined front is to consider the Fisher–Stefan model [47–52] that is obtained by re-formulating the usual Fisher–KPP model as a moving boundary problem:

$$\frac{\partial u}{\partial t} = \frac{\partial^2 u}{\partial x^2} + u(1 - u), \quad \text{on } 0 < x < L(t), \quad (5.1)$$

with $\partial u / \partial x = 0$ at $x = 0$ and $u(L(t), t) = 0$. Here, the sharp-front at the leading edge arises because of the homogeneous Dirichlet boundary condition. In the moving boundary framework, the position of the leading edge is explicitly determined as part of the solution and evolves according to a one-phase Stefan condition:

$$\frac{dL}{dt} = -\kappa \frac{\partial u}{\partial x}, \quad \text{at } x = L(t). \quad (5.2)$$

This boundary condition involves specifying a constant, κ , so that the velocity of the moving front is determined by both the choice of κ and $\partial u / \partial x$ at the moving front. In the heat and mass transfer literature, the constant κ is related to the Stefan number [45,46]. All travelling wave solutions of the Fisher–Stefan problem are sharp-fronted, and there is no longer the possibility of having smooth travelling wave solutions with this modelling framework.

Another point of interest is that the Fisher–KPP and Porous–Fisher models with initial conditions of the form (2.2) always lead to *invading* travelling wave solutions ($c > 0$). By contrast, we will demonstrate that the Fisher–Stefan model supports both invading travelling wave solutions by setting $\kappa > 0$ and receding travelling waves by setting $\kappa < 0$. For the special case of $\kappa = 0$, the Fisher–Stefan model leads to a stationary wave with $c = 0$ [49]. This flexibility in modelling biological invasion and recession is not possible with the Fisher–KPP or Porous–Fisher models. One interpretation of this difference is that the Fisher–Stefan model allows us to model a wider range of biologically plausible outcomes than either the Fisher–KPP or Porous–Fisher model [49,51].

It is worth noting that previous research has established various properties of the solution of the Fisher–Stefan model, such as existence and uniqueness [47,48], as well as stability considerations [52]. Our approach, as demonstrated for the Fisher–KPP and Porous–Fisher models in §§2 and 4, is to focus on using computational methods to explore time-dependent PDE solutions with the view to studying long-time travelling wave behaviour using a mixture of computational, phase plane and perturbation methods [49,51]. To illustrate our approach, we begin by solving equation (5.1) numerically by specifying initial condition of the form:

$$u(x, 0) = \begin{cases} u_0, & \text{if } 0 \leq x < L(0), \\ 0, & \text{if } x = L(0), \end{cases} \quad (5.3)$$

for some choice of $0 < u_0 \leq 1$. The first step is to transform the moving boundary problem to a fixed domain by writing $\rho = x/L(t)$, giving:

$$\frac{\partial u}{\partial t} = \frac{1}{L^2} \frac{\partial^2 u}{\partial \rho^2} + \frac{1}{L} \frac{dL}{dt} \frac{\partial u}{\partial \rho} + u(1-u), \quad \text{on } 0 < \rho < 1, \quad (5.4)$$

with $\partial u / \partial \rho = 0$ at $\rho = 0$ and $u(1, t) = 0$, and

$$\frac{dL}{dt} = -\frac{\kappa}{L} \frac{\partial u}{\partial \rho}, \quad \text{at } \rho = 1. \quad (5.6)$$

To solve the time-dependent PDE problem, we employ a uniform discretization of $0 < \rho < 1$ with grid spacing $\delta\rho$. Applying central difference approximations gives:

$$\frac{du_i}{dt} = \begin{cases} \frac{u_{i+1} - u_i}{(L\delta\rho)^2} + \frac{dL}{dt} \left[\frac{u_{i+1} - u_i}{L\delta\rho} \right] + u_i(1 - u_i), & \text{if } i = 1, \\ \frac{u_{i-1} - 2u_i + u_{i+1}}{(L\delta\rho)^2} + \frac{dL}{dt} \left[\frac{u_{i+1} - u_{i-1}}{2L\delta\rho} \right] + u_i(1 - u_i), & \text{if } 2 \leq i \leq N-1, \\ 0, & \text{if } i = N, \end{cases} \quad (5.5)$$

which is closed by discretizing the moving boundary condition:

$$\begin{aligned} \frac{dL}{dt} &= -\frac{\kappa}{L} \left[\frac{3u_N - 4u_{N-1} + u_{N-2}}{2\delta\rho} \right], \\ &= \frac{\kappa}{L} \left[\frac{4u_{N-1} - u_{N-2}}{2\delta\rho} \right], \end{aligned} \quad (5.7)$$

noting that $u_N = 0$ because of the homogeneous Dirichlet boundary condition at $\rho = 1$. Integrating these $N+1$ coupled nonlinear ODEs using DifferentialEquations.jl leads to time-dependent PDE solutions shown in figure 9, each with $u_0 = 0.5$ and $L(0) = 100$.

Simulations in figure 9a,b for $\kappa > 0$ lead to constant speed, constant shape invading travelling wave solutions moving in the positive x -direction. The travelling wave speed of these solutions can be estimated numerically like we did in figure 2 by tracking the position of some density contour and using regression. Since the Fisher–Stefan model is a moving boundary problem, there is a more obvious second approach to determine c as we can use our numerical estimates of u_{N-1} and u_{N-2} to evaluate (5.7) to give a direct estimate of dL/dt without needing to use front tracking and regression. Using this approach at $t = 1, 2, 3, \dots, 50$ indicates that dL/dt settles to a constant speed that agrees very well with the result obtained by front tracking and regression (not shown). In this section, we simply report estimates of c by evaluating equation (5.7) using late-time data. The two invading solutions in figure 9a,b indicate that c appears to increase with κ ; we will formalize the relationship between these quantities later when we turn to the phase plane. Interestingly, we have $c \approx 0.36$ for $\kappa = 1$ and $c \approx 0.666$ for $\kappa = 3$, indicating that these two travelling wave speeds are slower than the minimum travelling wave speed for the Fisher–KPP or Porous–Fisher models. Results in figure 9c,d for $\kappa < 0$ lead to receding travelling wave solutions with $c < 0$. Overall, we see that c is an increasing function of κ regardless of whether there is an invading or receding travelling wave; again we note that modelling biological recession is simply not possible using the Fisher–KPP or Porous–Fisher models, whereas in the moving boundary framework it is straightforward to model biological recession.

It is very interesting that travelling wave solutions of the Fisher–Stefan PDE model involve the same dynamical system as the Fisher–KPP model, namely:

$$\frac{dU}{dz} = V, \quad (5.8)$$

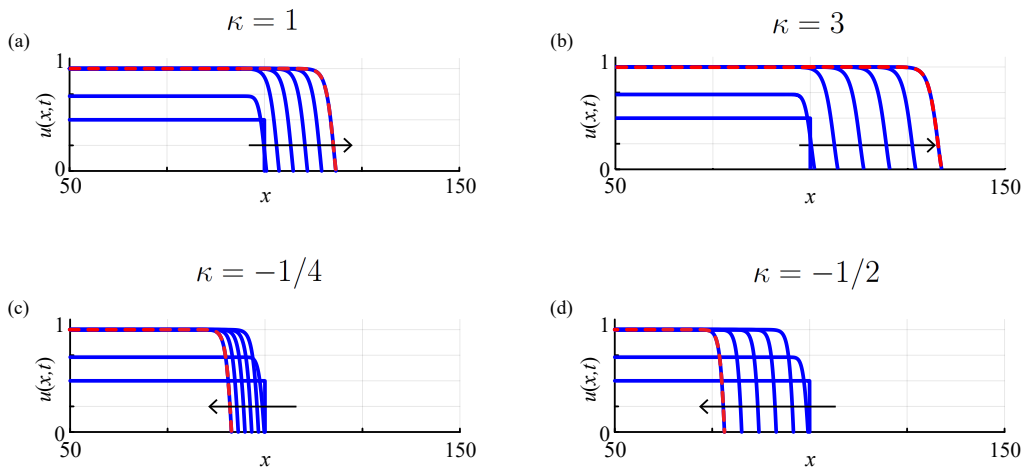


Figure 9. Time-dependent solutions of the Fisher–Stefan model illustrates how κ influences the long-time travelling wave speed c . Each subfigure shows a time-dependent PDE solution with the initial condition given by (5.3) with $u_0 = 0.5$ and $L(0) = 100$. Results show: (a) time-dependent PDE solution for $\kappa = 1$, which leads to an invading travelling wave with $c = 0.364421881$; (b) time-dependent PDE solution for $\kappa = 3$, which leads to an invading travelling wave with $c = 0.665977101$; (c) time-dependent PDE solution for $\kappa = -1/4$, which leads to a receding travelling wave with $c = -0.173023072$; and (d) time-dependent PDE solution for $\kappa = -1/2$, which leads to a receding travelling wave with $c = -0.442690692$. Each subfigure shows $u(x, t)$ (solid blue) at $t = 0, 1, 10, 20, 30, 40, 50$ with the arrow showing the direction of increasing time. All time-dependent PDE solutions are obtained with $\delta\rho = 2 \times 10^{-4}$, and each time-dependent PDE solution at $t = 50$ is superimposed with a dashed red line that corresponds to the shifted $U(z)$ profile obtained in the phase plane.

$$\frac{dV}{dz} = -cV - U(1 - U), \quad (5.9)$$

which we have already established has two equilibrium points $(\bar{U}, \bar{V}) = (0, 0)$ and $(\bar{U}, \bar{V}) = (1, 0)$, where $(\bar{U}, \bar{V}) = (1, 0)$ is a saddle point for all values of c . We have previously established that the origin is a stable spiral for $c < 2$, but we can anticipate from the time-dependent PDE solutions in figure 9 that the origin of the phase plane plays no role in these travelling wave solutions since the leading edge of the travelling wave has a negative finite slope, whereas a heteroclinic orbit entering the origin would have zero slope as $U \rightarrow 0$. We will now explore some specific phase planes to provide additional insight.

Results in figure 10 present numerically generated phase plane trajectories for $c = \pm 0.1$ and $c = \pm 0.5$. The upper panel in each subfigure shows the phase plane with the two equilibrium points highlighted, and special yellow trajectories entering and leaving the $(1, 0)$ equilibrium point along the stable and unstable manifolds. Each phase plane shows a red trajectory leaving the $(1, 0)$ equilibrium point along the unstable manifold into the fourth quadrant of the phase plane until it eventually intersects with the V -axis at a special point $(0, V^\dagger)$, which we highlight using a green square. The trajectory between $(1, 0)$ and $(0, V^\dagger)$ corresponds to the travelling wave solution; we have chosen to terminate this trajectory at the point where it intersects with the V -axis. Of course, since $c < 2$, we know from linear stability analysis that the trajectory will eventually spiral into the origin but we do not show this here as this part of the trajectory is not associated with the travelling wave solution from the time-dependent PDE model.

To develop analytical insight into these travelling waves, we re-write (5.8)–(5.9) as a single differential equation that directly describes the shape of the $V(U)$ trajectory in the (U, V) phase plane:

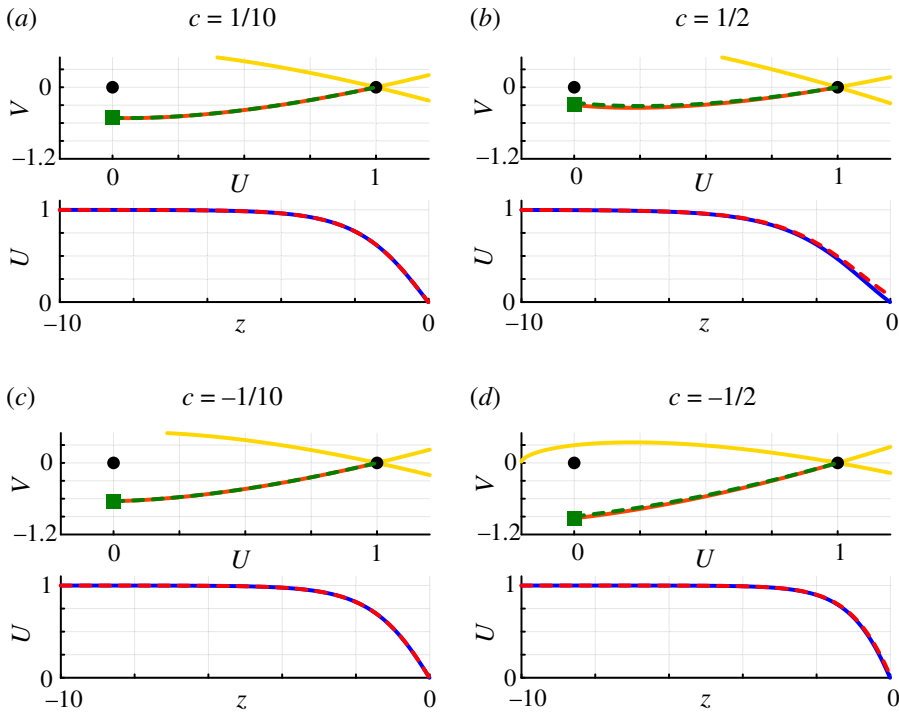


Figure 10. Phase planes for (5.8)–(5.9) and approximate perturbation solutions for slowly invading and slowly receding travelling wave solutions for the Fisher–Stefan model with $|c| \ll 1$: (a) $c = 0.1$; (b) $c = 0.5$; (c) $c = -0.1$; and (d) $c = -0.5$. The upper panel in each subfigure shows the phase plane where the equilibria are highlighted (black discs) and the special point $(0, V^\dagger)$ is also highlighted (green square). The red trajectory between $(1, 0)$ and $(0, V^\dagger)$ corresponds to the travelling wave solutions and an approximate perturbation solution for $|c| \ll 1$ superimposed. Results in the lower panel of each subfigure compare numerical estimates of the shape of the travelling wave (solid blue) with solutions obtained from the approximate perturbation solution (dashed red).

$$V(U) \frac{dV(U)}{dU} = -cV(U) - U(1-U), \quad V(1) = 0. \quad (5.10)$$

While we are unable to solve equation (5.10) to give a general expression for $V(U)$ for arbitrary values of c , we can solve for $V(U)$ in the special case $c = 0$ [61]. Our approach will be to use this result to construct a perturbation solution of the form:

$$V(U) = V_0(U) + cV_1(U) + \mathcal{O}(c^2). \quad (5.11)$$

Substituting (5.11) into (5.10) gives:

$$V_0(U) \frac{dV_0(U)}{dU} = -U(1-U), \quad V_0(1) = 0, \quad (5.12)$$

$$V_0(U) \frac{dV_1(U)}{dU} = -V_0(U) - V_1(U) \frac{dV_0(U)}{dU}, \quad V_1(1) = 0, \quad (5.13)$$

which can be solved to give:

$$V_0(U) = \pm \sqrt{\frac{2U^3 - 3U^2 + 1}{3}}, \quad (5.14)$$

$$V_1(U) = -\frac{(\sqrt{2U+1}[2U^2 - 3U - 2] + 3\sqrt{3})}{5\sqrt{2U+1}(U-1)}. \quad (5.15)$$

We choose the negative term in (5.14) since our numerical phase plane trajectories in figure 10 involve $V < 0$. Therefore, (5.15) is relevant for the negative square root in (5.14). We now have a two-term approximation $V(U) = V_0(U) + cV_1(U)$ describing the trajectory in the phase plane for $|c| \ll 1$. To illustrate how this approximation performs, we superimpose plots of $V_0(U) + cV_1(U)$ in each phase plane in figure 10 where we see that this approximate solution is visually indistinguishable from the full numerical solution of the dynamical system for $c = \pm 0.1$. By contrast, for $c = \pm 0.5$, we see a small difference between the perturbation solution and the full numerically generated trajectory, as we might expect.

To explore the relationship between κ and c , we evaluate our two-term perturbation expression at $U = 0$ to derive an expression for $V(0) = V^+$. Substituting this expression into the moving boundary condition:

$$\frac{dL}{dt} = -\kappa V^+, \quad (5.16)$$

gives a relationship between κ and c , noting that $dL/dt \rightarrow c$ as $t \rightarrow \infty$. Rearranging this expression gives

$$\kappa = \sqrt{3}c + \left(\frac{9\sqrt{3}-6}{5}\right)c^2 + \mathcal{O}(c^3), \quad (5.17)$$

confirming that c increases with κ for both slowly invading and receding travelling wave solutions with $|c| \ll 1$.

It is interesting to note that we have made analytic progress for slow-travelling wave solutions by developing approximate expressions for certain trajectories in the phase plane rather than working directly to obtain approximate expressions for $U(z)$ like we were able to do for fast-travelling wave solutions of the Fisher–KPP and Porous–Fisher models when $c \gg 1$. Our approach here of working in the phase plane is advantageous since we are able to use these perturbation solutions to derive an expression relating c to κ through the moving boundary condition. To compare the shape of the travelling wave solution $U(z)$ with our time-dependent PDE solutions, we take our numerical estimates of $U(V)$ and recall that $dU/dz = V$ by definition. Integrating this ODE numerically, again using the trapezoid rule, provides us with estimates of $U(z)$. This approach can be used to determine $U(z)$ either using the numerically generated phase plane trajectory for any value of c or the two-term perturbation approximation for $|c| \ll 1$. Using this approach, we computed $U(z)$ and compared the two profiles in the lower panel of each subfigure in figure 10. Here, we see that the perturbation approach leads to very accurate profiles of $U(z)$ for $c = \pm 0.1$. We also note that the late-time PDE solutions in figure 8 are superimposed with red dashed curves that are indistinguishable from the late-time PDE solution. These red dashed curves are obtained by generating the phase plane for the approximate value of c and using the $V(U)$ trajectory in the phase plane to estimate the $U(z)$ curve in the same way as described here.

Numerical simulations of time-dependent PDE solutions in figure 10c,d show PDE solutions with $\kappa < 0$ that lead to receding travelling wave solutions with $c < 0$. The shape of the $V(U)$ trajectories in the phase plane are given by equation (5.10), which has the property that $dV/dU = -c + U(1-U)/V \sim -c$ as $c \rightarrow -\infty$, suggesting that the relevant phase plane trajectories approach a straight line $V = c(U-1)$ as $c \rightarrow -\infty$. For this limiting straight line trajectory, we have $V(0) = V^+ = -c$ indicating that $\kappa \rightarrow -1^+$ as $c \rightarrow -\infty$. Note that for $\kappa < -1$, instead of evolving to a travelling wave profile, the time-dependent solution of equations (5.1)–(5.2) may undergo a form of finite-time blow-up [62], which is not the subject of this review.

To explore the shape of the travelling wave solution as $c \rightarrow -\infty$, we consider

$$\frac{1}{c} \frac{d^2U}{dz^2} + \frac{dU}{dz} + \frac{1}{c} U(1-U) = 0, \quad (5.18)$$

which is singular as $c \rightarrow -\infty$ and motivates us to consider a matched asymptotic expansion [60] treating c^{-1} as a small parameter. The boundary conditions for this problem are $U(0) = 0$ and $U(z) = 1$ as $z \rightarrow -\infty$. Setting $c^{-1} = 0$ and solving the resulting ODE gives the outer solution:

$$U(z) = 1, \quad (5.19)$$

to match the far-field boundary condition. We construct the inner solution near $z = 0$ by re-scaling the independent variable $\eta = cz$, giving

$$\frac{d^2U}{d\eta^2} + \frac{dU}{d\eta} + \frac{1}{c^2}U(1-U) = 0, \quad \text{on } -\infty < \eta < 0. \quad (5.20)$$

Treating c^{-1} as a small parameter, we seek a perturbation solution of the form $U(\eta) = U_0(\eta) + c^{-2}U_1(\eta) + \mathcal{O}(c^{-4})$, giving:

$$\frac{d^2U_0(\eta)}{d\eta^2} + \frac{dU_0(\eta)}{d\eta} = 0, \quad U_0(0) = 0, \quad U_0(\eta) = 1 \quad \text{as } \eta \rightarrow \infty, \quad (5.21)$$

$$\frac{d^2U_1(\eta)}{d\eta^2} + \frac{dU_1(\eta)}{d\eta} + U_0(\eta)(1-U_0(\eta)) = 0, \quad U_1(0) = 0, \quad U_1(\eta) = 0 \quad \text{as } \eta \rightarrow \infty. \quad (5.22)$$

The solution of these two boundary value problems, written in terms of the z variable, is:

$$U_0(z) = 1 - e^{-2cz}, \quad (5.23)$$

$$U_1(z) = \frac{1}{2}(e^{-2cz} + (2zc - 1)e^{-cz}), \quad (5.24)$$

gives us a two-term perturbation solution that directly approximates the shape of the travelling wave profile.

Recalling that $c \rightarrow -\infty$ as $\kappa \rightarrow -1^+$, we generate time-dependent PDE solutions, shown in figure 11, for $\kappa = -0.85$ and $\kappa = -0.90$. In both cases, we see that the initial profile forms a receding travelling wave with a steep boundary layer forming near $x = L(t)$. In each figure, we plot a late-time solution, focusing in on the shape of the leading edge over the interval $-10 \leq z \leq 0$ and compare the shape of the receding travelling wave generated by the time-dependent PDE solver with our two-term perturbation solution. As expected, we see some small discrepancy between the profiles when $\kappa = -0.85$, but the numerical and perturbation results are visually indistinguishable, at this scale, for $\kappa = -0.90$. The accuracy of the two-term matched asymptotic perturbation solution in figure 11b is remarkable given that this approximation is valid in the limit $c \rightarrow -\infty$ and yet we find it provides a reasonable approximation for just $c \approx -1.95$.

In addition to providing an understanding of the shape of fast receding travelling wave solutions, our perturbation solutions also provide insight into the relationship between c and κ as $c \rightarrow -\infty$. For all travelling wave solutions, we have $\kappa = -c/V(0)$, and as $c \rightarrow -\infty$, we can estimate $V(0)$ using our perturbation solutions by evaluating $\kappa = -c/dU/dz$ at $z = 0$ by differentiating our expressions for $U_0(z)$ and $U_1(z)$ with respect to z and evaluating the resulting expressions at $z = 0$, giving:

$$\kappa = -1 + \frac{1}{2c^2} + \mathcal{O}\left(\frac{1}{c^4}\right), \quad (5.25)$$

which shows precisely how κ relates to c as $c \rightarrow -\infty$. These results for $c \rightarrow -\infty$ correspond to $\kappa \rightarrow -1^+$. Time-dependent PDE solutions can be generated for $\kappa \leq -1$, but in this case, we see the formation of receding fronts that appear to accelerate in the negative x -direction rather than settle to a constant speed travelling wave solution [62].

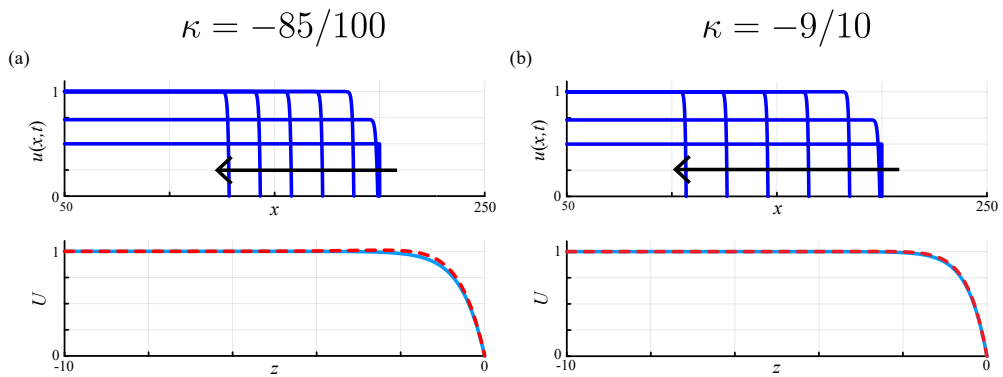


Figure 11. Fast receding travelling wave solutions of the Fisher–Stefan model for (a) $\kappa = -0.85$; and (b) $\kappa = -0.90$. Results in the upper panel show time-dependent PDE solutions evolving from $u_0 = 0.5$ and $L(0) = 200$. Profiles are shown at $t = 0, 1, 10, 20, 30, 40, 50$ with the arrow showing the direction of increasing time. These numerical results indicate that we have $c = -1.482746707$ for $\kappa = -0.85$ and $c = -1.948448670$ for $\kappa = -0.90$. Results in the lower panel compare the shape of the travelling wave profiles estimated from late-time PDE solutions (solid blue) and the two-term perturbation solution (dashed red). All time-dependent PDE solutions are obtained with $\delta\rho = 2 \times 10^{-4}$.

Before concluding our discussion about the Fisher–Stefan model it is insightful to note that using both the time-dependent PDE model and phase plane tools provides us with opportunities to independently check the accuracy of our numerical algorithms. For example, generating the time-dependent PDE solutions in figure 9 involves specifying κ as an input and observing c as an output. This process involves several different approximations since we must discretize the governing PDE, solve the resulting system of semi-discrete ODEs for a sufficiently long period of time before using the discretized boundary condition to provide estimate c . For example, time-dependent solutions in figure 9a involve specifying $\kappa = 1$, and our estimate of $c = 0.364421881$ is impacted by several choices we have made in implementing our numerical algorithm, such as truncation error. One way of testing the accuracy of our approximation is to repeat the calculation by resolving the time-dependent PDE model on a finer mesh and examine how our estimate of c depends upon the choice of $\delta\rho$. A different approach is to use the phase plane where we specify c as an input, generate the trajectory leaving $(1, 0)$ along the unstable manifold and to use this trajectory to estimate V^\dagger , from which we can apply the moving boundary condition, $c = -\kappa V^\dagger$ to give κ as an output of the phase plane calculations. To demonstrate this approach, we generated the phase plane with $c = 0.364421881$ as an input, solved for the appropriate trajectory to give $V^\dagger = -0.365356934$, and then applied the moving boundary condition to find that $\kappa = 0.997440708$, which is within 0.26% of the expected result, $\kappa = 1$. This intercode comparison is convenient since it gives us confidence that both the time-dependent PDE algorithm and the numerical phase plane algorithm are giving consistent results. In addition, if we repeat this intercode comparison by resolving the time-dependent PDE model with more mesh points we obtain an improved estimate of c , which, when used as an input into the phase plane, leads to an improved estimate of κ (results not shown).

Another point of interest about the Fisher–Stefan model is that our results in figure 9 all lead to long-time travelling wave solutions. There is another possibility that we have not focused on in this review, which is motivated by the observation that the boundary condition $u(L(t), t) = 0$ is associated with a diffusive loss of material at $x = L(t)$, where the outward flux is $\mathcal{J} = -\partial u / \partial x$. This loss of material can lead to the population going extinct and $u \rightarrow 0$ as $t \rightarrow \infty$ [47,49]. These two different outcomes have given rise to what has been called the *spreading–vanishing dichotomy* for the Fisher–Stefan model [47,49]. The eventual growth or extinction of the initial population is governed by the diffusive loss at $u = L(t)$ and the increase in mass driven by the

logistic source term, and the balance of these two processes is determined by the initial length of the population, $L(0)$. Simple conservation arguments show that $L(0) > \pi/2$ lead to spreading and long-time travelling wave behaviour, whereas $L(0) < \pi/2$ leads to eventual extinction of the population. Since this review focuses on travelling wave solutions, we have intentionally focused on time-dependent PDE solutions with $L(0) > \pi/2$; however, our time-dependent PDE codes available on [GitHub](#) can be used to explore different initial conditions leading to extinction simply by changing $L(0)$. Details of the analysis explaining how to arrive at the critical value of $L(0) = \pi/2$ are provided in our previous work [49].

6. Discussion

In this review, we have presented open access computational tools written in JULIA for three reaction–diffusion models of biological invasion, namely the Fisher–KPP, Porous–Fisher and Fisher–Stefan models. The first of these, the Fisher–KPP model, is very well studied in the literature, while the latter two can be motivated in part to address certain limitations of the Fisher–KPP model, including the preference for well-defined fronts and the possibility of invading of receding populations. We anticipate that these computational tools could be used to support senior undergraduate and graduate-level teaching and learning about mathematical modelling of biological invasion. Moreover, we anticipate that the computational tools will be straightforward to adapt to other reaction–diffusion models, as required. For each PDE model, we generate time-dependent solutions, paying particular attention to relate late-time PDE solutions to properties of the travelling wave phase plane. Using perturbation methods, we provide mathematical insight into the shape of various travelling wave solutions in certain asymptotic limits. Using a range of computation and visualization, we relate these approximate solutions to numerical solutions of the full PDE problems. Finally, in appendix A, we include equivalent details for an additional model, the Porous–Fisher–Stefan model, that combined features of the Porous–Fisher and Fisher–Stefan models.

This review deliberately focuses on three important types of reaction–diffusion models of biological invasion. It is obvious that there are many opportunities for extending the material in this review. For example, we do not discuss any source terms other than logistic growth; however, it is relatively straightforward to implement different forms of sigmoid source terms in the time-dependent PDE algorithms, such as the broad family of generalized logistic source terms reviewed by Tsoularis & Wallace [25]. These modified algorithms can be used to explore how the resulting travelling wave solutions and their interpretation in the phase plane. Another clear restriction in this review is that we only consider nonlinear degenerate diffusion of the form $\mathcal{J} = -u \partial u / \partial x$, whereas others have considered more general terms such as $\mathcal{J} = -u^m \partial u / \partial x$ for some exponent $m > 0$ [3,10,40]. Both of these generalizations can be explored by adapting the open source computational tools provided as part of this review.

A more mathematically challenging but biologically realistic extension of the work covered in this review is to relax the constraint of focusing on scalar reaction–diffusion models. Working with coupled problems, sometimes called *multi-species* models, brings new opportunities for developing more realistic mathematical models as real applications of biological invasions typically involve interactions of multiple subpopulations. Multi-species models have been formulated and analysed from the point of view of considering general interactions between different subpopulations [63] as well as more specific models of biological processes such as trophoblast invasion during pregnancy [64], malignant invasion into surrounding tissues [18,21] and many more. Such multi-species models can be formulated either as classical PDE problems that directly generalize the Fisher–KPP model, or as multi-species analogues of moving boundary problems similar to the Fisher–Stefan model. While extending the computational tools provided here for solving time-dependent PDE models is relatively straightforward for multi-species models, our ability to extend the phase plane tools becomes limited.

For example, travelling wave solutions arising in a two-species reaction–diffusion model of biological invasion typically lead to a four-dimensional phase space problem that is far more difficult to analyse as a dynamical system and more challenging to visualize than the types of simpler phase planes explored here.

Ethics. This work did not require ethical approval from a human subject or animal welfare committee.

Data accessibility. All algorithms that generate the computational data are available on GitHub at [65].

Declaration of AI use. We have not used AI-assisted technologies in creating this article.

Authors' contributions. M.J.S.: conceptualization, formal analysis, funding acquisition, investigation, methodology, project administration, resources, software, validation, visualization, writing—original draft, writing—review and editing; SWM: conceptualization, formal analysis, writing-review and editing.

Both authors gave final approval for publication and agreed to be held accountable for the work performed therein.

Conflict of interest declaration. We declare we have no competing interests.

Funding. This work is supported by the Australian Research Council (DP230100025).

Acknowledgements. We thank Emeritus Professor Sean McElwain and two referees for helpful comments.

Dedication. Matthew Simpson dedicates this work to his former colleague, co-author and good friend, Francis E. Yeomans (1941–2020).

Appendix A: Porous–Fisher–Stefan model

As we point out in the main document, two common approaches for developing simple reaction–diffusion models that lead to sharp-fronted travelling waves are to either introduce a degenerate nonlinear diffusion mechanism into the classical Fisher–KPP model or to re-formulate the Fisher–KPP model as a moving boundary problem. Interestingly, it is also possible to combine both of these approaches by reformulating the Porous–Fisher model as a moving boundary problem:

$$\frac{\partial u}{\partial t} = \frac{\partial}{\partial x} \left[u \frac{\partial u}{\partial x} \right] + u(1-u), \quad \text{on } 0 < x < L(t), \quad (\text{A } 1)$$

with $\partial u / \partial x = 0$ at $x = 0$ and $u(L(t), t) = 0$. As for the Fisher–Stefan model, we have a moving boundary problem where $L(t)$ is determined as part of the solution by specifying [53]:

$$\frac{dL}{dt} = -\kappa u \frac{\partial u}{\partial x} \quad \text{at } x = L(t). \quad (\text{A } 2)$$

This model has been referred to as the Porous–Fisher–Stefan model [53]. Similar to the Fisher–Stefan model, here, the moving boundary condition involves specifying a constant κ that determines the velocity of the leading edge. The Porous–Fisher–Stefan model is closely related to both the Porous–Fisher and Fisher–Stefan models; accordingly, our analysis of travelling wave solutions of the Porous–Fisher–Stefan model will borrow ideas previously employed for the Porous–Fisher and Fisher–Stefan models. As we will show later, as the velocity of the moving boundary in the Porous–Fisher–Stefan model is finite, (A 2) implies that the gradient of the density profile, $\partial u / \partial x$, must be infinite at the leading edge as we have $u(L(t), t) = 0$.

To explore time-dependent solutions of the Porous–Fisher–Stefan model, we introduce a transformed variable $\phi = u^2$, for $\phi \geq 0$, which gives:

$$\frac{\partial \phi}{\partial t} = \sqrt{\phi} \frac{\partial^2 \phi}{\partial x^2} + 2\phi(1-\sqrt{\phi}), \quad \text{on } 0 < x < L(t), \quad (\text{A } 3)$$

with $\partial \phi / \partial x = 0$ at $x = 0$ and $\phi(L(t), t) = 0$. Re-writing the time-dependent PDE in terms of ϕ may, at first, seem unhelpful since the PDE is re-cast in an unfamiliar form that cannot be written as a standard conservation PDE. The benefit of working in the ϕ variable becomes clear when we consider the moving boundary condition:

$$\frac{dL}{dt} = -\frac{\kappa}{2} \frac{\partial \phi}{\partial x} \quad \text{at} \quad x = L(t), \quad (\text{A } 4)$$

which avoids the $0 \times \infty$ indeterminate form in (A 2) for the original u variable. To solve the moving boundary problem for $\phi(x, t)$ numerically, we first transform to the fixed boundary by writing $\rho = x/L(t)$, which gives:

$$\frac{\partial \phi}{\partial t} = \frac{\sqrt{\phi}}{L^2} \frac{\partial^2 \phi}{\partial \rho^2} + \frac{1}{L} \frac{dL}{dt} \frac{\partial \phi}{\partial \rho} + 2\phi(1 - \sqrt{\phi}), \quad \text{on} \quad 0 < \rho < 1, \quad (\text{A } 5)$$

with $\partial \phi / \partial \rho = 0$ at $\rho = 0$ and $\phi(1, t) = 0$. In the fixed-domain coordinates, we have:

$$\frac{dL}{dt} = -\frac{\kappa}{2L} \frac{\partial \phi}{\partial \rho} \quad \text{at} \quad \rho = 1. \quad (\text{A } 6)$$

To solve the time-dependent PDE problem, we consider a uniform discretization of $0 < \rho < 1$ with grid spacing $\delta\rho$. Applying central difference approximations gives:

$$\frac{d\phi_i}{dt} = \begin{cases} \frac{\sqrt{\phi_i}(\phi_{i+1} - \phi_i)}{(L\delta\rho)^2} + \frac{dL}{dt} \left[\frac{\phi_{i+1} - \phi_i}{L\delta\rho} \right] + 2\phi_i(1 - \sqrt{\phi_i}), & \text{if } i = 1, \\ \frac{\sqrt{\phi_i}(\phi_{i-1} - 2\phi_i + \phi_{i+1})}{(L\delta\rho)^2} + \frac{dL}{dt} \left[\frac{\phi_{i+1} - \phi_{i-1}}{2L\delta\rho} \right] + 2\phi_i(1 - \sqrt{\phi_i}), & \text{if } 2 \leq i \leq N-1, \\ 0, & \text{if } i = N, \end{cases} \quad (\text{A } 7)$$

which is closed by specifying

$$\begin{aligned} \frac{dL}{dt} &= -\frac{\kappa}{2L} \left[\frac{3\phi_N - 4\phi_{N-1} + \phi_{N-2}}{2\delta\rho} \right], \\ &= \frac{\kappa}{2L} \left[\frac{4\phi_{N-1} - u_{N-2}}{2\delta\rho} \right], \end{aligned} \quad (\text{A } 8)$$

noting that $\phi_N = 0$ by definition. This system of $N+1$ coupled nonlinear ODEs can be integrated through time using DifferentialEquations.jl to give estimates of $\phi(\rho, t)$ and $L(t)$. Recalling that $u = +\sqrt{\phi}$, we can plot the solution in terms of $u(x, t)$. Note that the appropriate boundary condition on the moving boundary is to enforce $u(L(t), t) = 0$. Computationally, however, it is necessary to approximate this as $u(L(t), t) = U$, with $U \ll 1$, otherwise the discretized system of ODEs does not evolve with time. All numerical results in figure 12 are obtained by setting $\phi(L(t), t) = 1 \times 10^{-8}$. These time-dependent PDE results are reminiscent of those in figure 9 for the Fisher–Stefan problem as we see a series of sharp-fronted moving fronts that, in the long-time limit, approach a constant speed and constant shape travelling wave. Moreover, we see that setting $\kappa > 0$ leads to invading travelling waves with $c > 0$, whereas setting $\kappa < 0$, we obtain receding travelling waves with $c < 0$.

To study the travelling wave solutions of the Porous–Fisher–Stefan model, we turn to the phase plane. Working in the travelling wave coordinate $z = x - ct$, we note that travelling wave solutions are invariant with respect to a translation in z , so we are free to choose $z = 0$ to represent the location of the moving boundary, which gives:

$$\sqrt{\phi} \frac{d^2 \phi}{dz^2} + c \frac{d\phi}{dz} + 2\phi(1 - \sqrt{\phi}) = 0, \quad \text{on} \quad -\infty < z < 0, \quad (\text{A } 9)$$

with boundary conditions

$$\lim_{z \rightarrow -\infty} \phi(z) = 1, \quad \phi(0) = 0, \quad \text{and} \quad \lim_{z \rightarrow 0^-} \frac{d\phi}{dz} = -\frac{2c}{\kappa}. \quad (\text{A } 10)$$

We explore solutions to this boundary value problem by considering the (ϕ, ψ) phase plane:

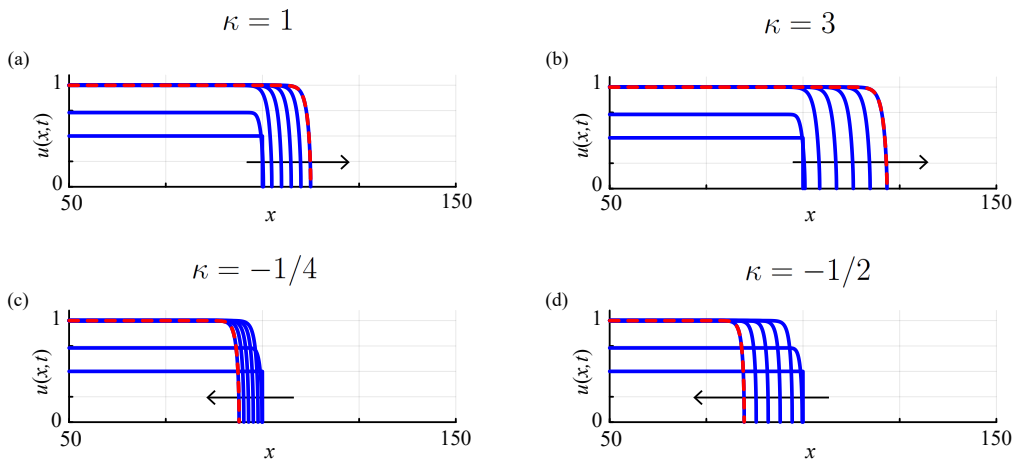


Figure 12. Time-dependent solutions of the Porous–Fisher–Stefan model illustrates how κ influences the long-time travelling wave speed c . Each subfigure shows a time-dependent PDE solution with the initial condition given by (5.3) with $u_0 = 0.5$ and $L(0) = 100$. Results show: (a) time-dependent PDE solution for $\kappa = 1$, which leads to an invading travelling wave with $c = 0.251165418$; (b) time-dependent PDE solution for $\kappa = 3$, which leads to an invading travelling wave with $c = 0.435671955$; (c) time-dependent PDE solution for $\kappa = -1/4$, which leads to a receding travelling wave with $c = -0.122673575$; and (d) time-dependent PDE solution for $\kappa = -1/2$, which leads to a receding travelling wave with $c = -0.310757910$. Each subfigure shows $u(x, t)$ (solid blue) at $t = 0, 1, 10, 20, 30, 40, 50$ with the arrow showing the direction of increasing time. All time-dependent PDE solutions are obtained with $\delta\rho = 2 \times 10^{-4}$, and each time-dependent PDE solution at $t = 50$ is superimposed with a dashed red line that corresponds to the shifted $U(z)$ profile obtained in the phase plane.

$$\frac{d\phi}{dz} = \psi, \quad (\text{A } 11)$$

$$\frac{d\psi}{dz} = -\frac{c\psi}{\sqrt{\phi}} - 2\sqrt{\phi}(1 - \sqrt{\phi}). \quad (\text{A } 12)$$

We are unable to find exact solutions of equations (A 11)–(A 12) for arbitrary values of c . Instead, inspired by our approach for studying travelling waves of the Fisher–Stefan model, we re-write equations (A 11)–(A 12) as an ODE that describes the trajectory shape $\psi(\phi)$, in the (ϕ, ψ) phase plane, giving:

$$\frac{d\psi(\phi)}{d\phi} = -\frac{c}{\sqrt{\phi}} - \frac{2\sqrt{\phi}(1 - \sqrt{\phi})}{\psi(\phi)}, \quad \psi(1) = 0, \quad \lim_{\phi \rightarrow 0^+} \psi(\phi) = -\frac{2c}{\kappa}. \quad (\text{A } 13)$$

As noted in §3, travelling wave solutions of the Porous–Fisher model only occur for $c \geq 1/\sqrt{2}$ and our numerical exploration of time-dependent PDE solutions for the Porous–Fisher–Stefan model in figure 12 suggests that we have travelling wave solutions with $c < 1/\sqrt{2}$. Guided by our experience with the Fisher–Stefan model in §5, we note that it is possible to find an exact solution of (A 13) for the special case of $c = 0$. These two observations motivate us to consider (A 13) in two asymptotic limits: $c \rightarrow 0$ and $c \rightarrow 1/\sqrt{2}^-$.

To explore solutions of (A 13) for $|c| \ll 1$, we expand $\psi(\phi)$ in a regular perturbation expansion:

$$\psi(\phi) = \psi_0(\phi) + c\psi_1(\phi) + \mathcal{O}(c^2), \quad (\text{A } 14)$$

which, when substituted into (A 13), gives:

$$\psi_0(\phi) \frac{d\psi_0(\phi)}{d\phi} = -2\sqrt{\phi}(1-\sqrt{\phi}), \quad \psi_0(1) = 0, \quad (\text{A } 15)$$

$$\psi_0(\phi) \frac{d\psi_1(\phi)}{d\psi} = -\psi_1(\phi) \frac{d\psi_0(\phi)}{d\psi} - \frac{\psi_0(\phi)}{\sqrt{\phi}}, \quad \psi_1(1) = 0, \quad (\text{A } 16)$$

with exact solutions

$$\psi_0(\phi) = \pm \sqrt{\frac{2-8\phi^{3/2}+6\phi^2}{3}}, \quad (\text{A } 17)$$

$$\psi_1(\phi) = -\frac{1}{\psi_0(\phi)} \int_{\phi}^1 \sqrt{\frac{2-8s^{3/2}+6s^2}{3s}} ds, \quad (\text{A } 18)$$

where the integral in (A 18) can be evaluated using quadrature. Results in figure 13 compare a range of phase planes and associated travelling wave profile shapes for $c = \pm 0.1$ and $c = \pm 0.5$. The upper panel in each subfigure shows the (ϕ, ψ) phase plane with a numerical trajectory obtained by solving (A 13) using DifferentialEquations.jl in JULIA. Each trajectory leaves the $(1, 0)$ saddle point along the unstable manifold into the fourth quadrant, eventually intersecting the ψ axis at a special point denoted with the green square. Each phase plane also includes a plot of the two-term perturbation solution $\psi_0(\phi) + c\psi_1(\phi)$, which gives curves that are indistinguishable from the numerically generated trajectories for $c = \pm 0.1$, whereas there is a small difference between the two trajectories for $c = \pm 0.5$, as expected. As for the Fisher–Stefan phase plane analysis in figure 10, we use numerical integration to construct the $\phi(z)$ profile from the phase plane trajectories, and these profiles are then plotted as $U(z) = \sqrt{\phi(z)}$ in the lower panel of each subfigure where we compare the shape of the travelling wave profile obtained using a numerical solution and perturbation solutions of (A 13).

Evaluating our two-term perturbation solution at $\phi = 0$ allows us to relate c and κ through the moving boundary condition, which gives:

$$\kappa = \sqrt{6}c + \frac{\alpha\sqrt{3}}{27}c^2 + \mathcal{O}(c^3), \quad (\text{A } 19)$$

where $\alpha = 36\sqrt{2} - 6\sqrt{3} + 24\ln[(\sqrt{3}-1)/(3\sqrt{2}-4)] \approx 67.02$. A notable feature of the phase planes in figure 13 is that ψ remains $\mathcal{O}(1)$ as $\phi \rightarrow 0^+$. Noting that $\phi = U^2$ and $\psi = 2UdU/dz$, then $dU/dz = \mathcal{O}(U^{-1})$ as $U \rightarrow 0^+$ confirming that dU/dz is infinite at $z = 0$. This property is very different to sharp-fronted solutions of the Porous–Fisher model or the Fisher–Stefan model. In both these previous cases, dU/dz is finite at the leading edge of the population. This is a new feature that the previous models covered in this review do not share.

For the special travelling wave speed $c = 1/\sqrt{2}$, (A 13) has the solution that $dU/dz = (U-1)/\sqrt{2}$, meaning that $\psi = 2UdU/dz \rightarrow 0$ as $U \rightarrow 0^+$. The moving boundary condition requires that the quantity $-2c/\kappa$ is zero, and since $c > 0$, we must have $\kappa \rightarrow \infty$ as $c \rightarrow 1/\sqrt{2}^-$. The leading-order behaviour of this limit can be explored by writing $c = 1/\sqrt{2} - \varepsilon$, for $\varepsilon \ll 1$ so that (A 13) can be written as:

$$\frac{d\psi(\phi)}{d\phi} = \frac{\varepsilon}{\sqrt{\phi}} - \frac{1}{\sqrt{2}\phi} - \frac{2\sqrt{\phi}(1-\sqrt{\phi})}{\psi(\phi)}, \quad \psi(1) = 0, \quad \lim_{\phi \rightarrow 0^+} \psi(\phi) = -\frac{2}{\kappa} \left(\frac{1}{\sqrt{2}} - \varepsilon \right). \quad (\text{A } 20)$$

Substituting a regular perturbation solution of the form:

$$\psi(\phi) = \psi_0(\phi) + \varepsilon\psi_1(\phi) + \mathcal{O}(\varepsilon^2), \quad (\text{A } 21)$$

into (A 20) gives:

$$\frac{d\psi_0(\phi)}{d\phi} = -\frac{1}{\sqrt{2}\phi} - \frac{2\sqrt{\phi}(1-\sqrt{\phi})}{\psi_0(\phi)}, \quad \psi_0(1) = 0, \quad (\text{A } 22)$$

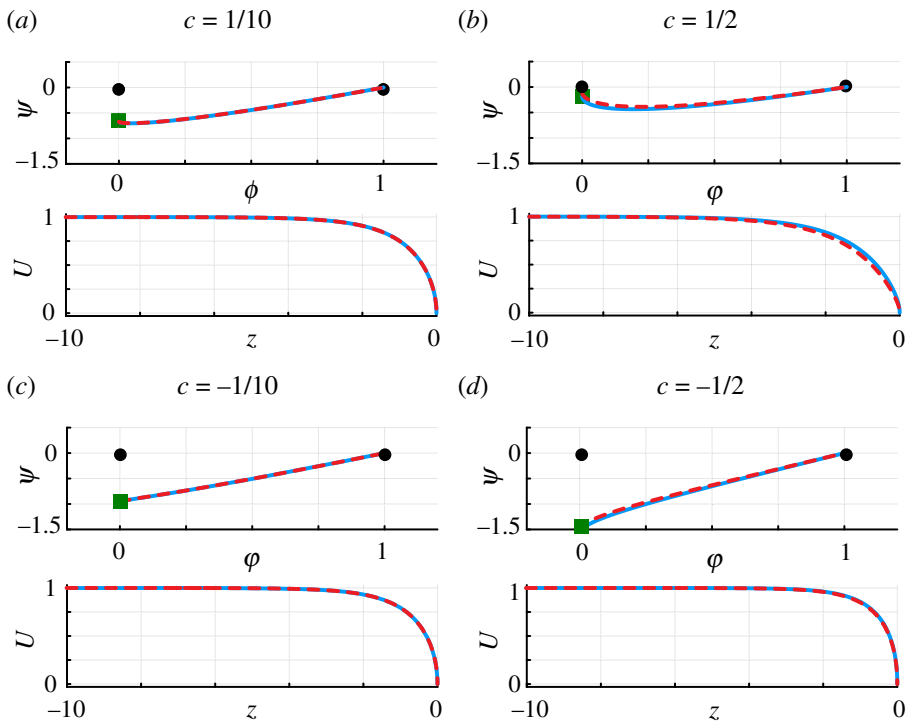


Figure 13. Phase planes for (A 11)–(A 12) and approximate perturbation solutions for slowly invading and slowly receding travelling wave solutions for the Porous–Fisher–Stefan model with $|c| \ll 1$: (a) $c = 0.1$; (b) $c = 0.5$; (c) $c = -0.1$; and (d) $c = -0.5$. The upper panel in each subfigure shows the phase plane where the equilibria are highlighted (black discs) and the special point $(0, \psi^\dagger)$ is also highlighted (green square). The red trajectory between $(1, 0)$ and $(0, \psi^\dagger)$ corresponds to the travelling wave solutions and an approximate perturbation solution for $|c| \ll 1$ is superimposed. Results in the lower panel of each subfigure compare numerical estimates of the shape of the travelling wave (solid blue) with solutions obtained from the approximate perturbation solution (dashed red).

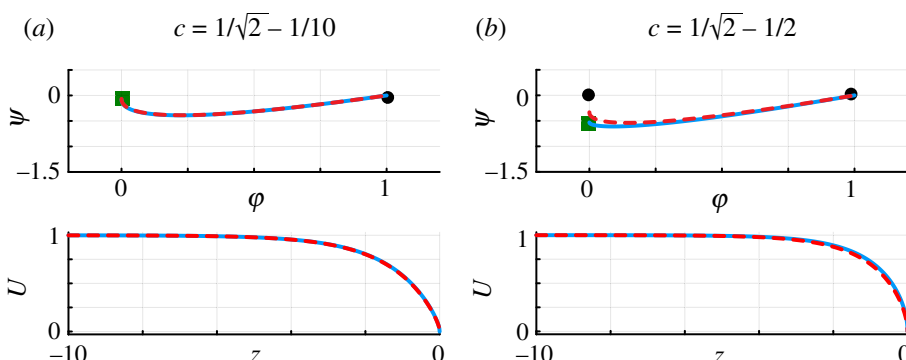


Figure 14. Phase planes for (A 11)–(A 12) and approximate perturbation solutions for $c = 1/\sqrt{2} - \varepsilon$: (a) $\varepsilon = 1/10$; (b) $\varepsilon = 1/2$. The upper panel in both subfigures shows the phase plane where the equilibria are highlighted (black discs) and the special point $(0, \psi^\dagger)$ is also highlighted (green square). The red trajectory between $(1, 0)$ and $(0, \psi^\dagger)$ corresponds to the travelling wave solutions and an approximate perturbation solution for $c - 1/\sqrt{2} \ll 1$ is superimposed. Results in the lower panel of each subfigure compare numerical estimates of the shape of the travelling wave (solid blue) with solutions obtained from the approximate perturbation solution (dashed red).

$$\psi_0(\phi) \frac{d\psi_1(\phi)}{d\psi} = -\psi_1(\phi) \frac{d\psi_0(\phi)}{d\psi} - \frac{\psi_1(\phi)}{\sqrt{2}\phi} + \frac{\psi_0(\phi)}{\sqrt{\phi}}, \quad \psi_1(1) = 0, \quad (\text{A } 23)$$

with exact solutions

$$\psi_0(\phi) = -\sqrt{2\phi}(1 - \sqrt{\phi}), \quad (\text{A } 24)$$

$$\psi_1(\phi) = -\frac{2(1 - \sqrt{\phi})}{3}. \quad (\text{A } 25)$$

Results in figure 14 explore the accuracy of this limit by generating phase planes for $c = 1/\sqrt{2} - \varepsilon$ for $\varepsilon = 0.1, 0.5$ where we see the numerically generated trajectory obtained by solving (A 13) using DifferentialEquations.jl is visually indistinguishable from our two-term perturbation solution for $\varepsilon = 0.1$, whereas we see some small discrepancy between the trajectories for $\varepsilon = 0.5$. The lower panel in each subfigure compares the numerically generated phase plane trajectories with the two-term perturbation solution in terms of the $U(z)$ travelling wave profiles.

Evaluating our two-term perturbation solution at $\phi = 0$ gives:

$$\kappa = \frac{3\sqrt{2}c}{1 - \sqrt{2}c} + \mathcal{O}\left(c - \frac{1}{\sqrt{2}}\right)^3, \quad (\text{A } 26)$$

which shows how κ relates to c for $\kappa \gg 1$ and $c \rightarrow 1/\sqrt{2}^-$.

References

1. Steele J, Adams J, Sluckin T. 1998 Modelling paleoindian dispersals. *World Archaeol.* **30**, 286–305. (doi:10.1080/00438243.1998.9980411)
2. Acevedo MA, Marcano M, Fletcher RJ. 2012 A Diffusive logistic growth model to describe forest recovery. *Ecol. Model.* **244**, 13–19.
3. Jin W, Shah ET, Penington CJ, McCue SW, Chopin LK, Simpson MJ. 2016 Reproducibility of scratch assays is affected by the initial degree of confluence: experiments, modelling and model selection. *J. Theor. Biol.* **390**, 136–145. (doi:10.1016/j.jtbi.2015.10.040)
4. Simpson MJ, Murphy RJ, Maclarens OJ. 2024 Modelling count data with partial differential equations models in biology. *J. Theor. Biol.* **580**, 111732. (doi:10.1016/j.jtbi.2024.111732)
5. Skellam JG. 1951 Random dispersal in theoretical populations. *Biometrika* **38**, 196–218. (doi:10.1093/biomet/38.1-2.196)
6. Shigesada N, Kawasaki K, Takeda Y. 1995 Modeling stratified diffusion in biological invasions. *Am. Nat.* **146**, 229–251. (doi:10.1086/285796)
7. Kot M. 2003 *Elements of mathematical ecology*. Cambridge, UK: Cambridge University Press.
8. Edelstein-Keshet L. 2005 *Mathematical models in biology*. Philadelphia, PA: SIAM. See <http://pubs.siam.org/doi/book/10.1137/1.9780898719147>.
9. Murray JD. 2002 *Mathematical biology I. An introduction*. New York, NY: Springer.
10. Sherratt JA, Murray JD. 1990 Models of epidermal wound healing. *Proc. Biol. Sci.* **241**, 29–36. (doi:10.1098/rspb.1990.0061)
11. Maini PK, McElwain DLS, Leavesley DI. 2004 Traveling wave model to interpret a wound-healing cell migration assay for human peritoneal mesothelial cells. *Tissue Eng.* **10**, 475–482. (doi:10.1089/107632704323061834)
12. Maini PK, McElwain DLS, Leavesley D. 2004 Travelling waves in a wound healing assay. *Appl. Math. Lett.* **17**, 575–580. (doi:10.1016/S0893-9659(04)90128-0)
13. Cai AQ, Landman KA, Hughes BD. 2007 Multi-scale modeling of a wound-healing cell migration assay. *J. Theor. Biol.* **245**, 576–594. (doi:10.1016/j.jtbi.2006.10.024)
14. Sengers BG, Please CP, Oreffo ROC. 2007 Experimental characterization and computational modelling of two-dimensional cell spreading for skeletal regeneration. *J. R. Soc. Interface* **4**, 1107–1117. (doi:10.1098/rsif.2007.0233)

15. Landman KA, Pettet GJ, Newgreen DF. 2003 Mathematical models of cell colonization of uniformly growing domains. *Bull. Math. Biol.* **65**, 235–262. (doi:10.1016/S0092-8240(02)00098-8)
16. Simpson MJ, Landman KA, Hughes BD, F. Newgreen D. 2006 Looking inside an invasion wave of cells using continuum models: proliferation is the key. *J. Theor. Biol.* **243**, 343–360. (doi:10.1016/j.jtbi.2006.06.021)
17. Di Talia S, Vergassola M. 2022 Waves in embryonic development. *Annu. Rev. Biophys.* **51**, 327–353. (doi:10.1146/annurev-biophys-111521-102500)
18. Gatenby RA, Gawlinski ET. 1996 A reaction–diffusion model of cancer invasion. *Cancer Res.* **56**, 5745–5753. <https://aacrjournals.org/cancerres/article-pdf/56/24/5745/2462558/cr0560245745.pdf>
19. Perumpanani AJ, Sherratt JA, Norbury J, Byrne HM. 1999 A two parameter family of travelling waves with a singular barrier arising from the modelling of matrix mediated malignant invasion. *Physica D: Nonlinear Phenomena* **126**, 145–159. (doi:10.1016/S0167-2789(98)00272-3)
20. Swanson KR, Bridge C, Murray JD, Alvord EC. 2003 Virtual and real brain tumors: using mathematical modeling to quantify glioma growth and invasion. *J. Neurol. Sci.* **216**, 1–10. (doi:10.1016/j.jns.2003.06.001)
21. Browning AP, Haridas P, Simpson MJ. 2019 A Bayesian sequential learning framework to parameterise continuum models of melanoma invasion into human skin. *Bull. Math. Biol.* **81**, 676–698. (doi:10.1007/s11538-018-0532-1)
22. Fisher RA. 1937 The wave of advance of advantageous genes. *Ann. Eugen.* **7**, 355–369. (doi:10.1111/j.1469-1809.1937.tb02153.x)
23. Kolmogorov AN, Petrovskii IG, Piskunov NS. 1937 A study of the diffusion equation with increase in the amount of substance, and its application to a biological problem. *Moscow Univ. Math. Bull.* **1**, 1–26.
24. Richards FJ. 1959 A flexible growth function for empirical use. *J. Exp. Bot.* **10**, 290–301. (doi:10.1093/jxb/10.2.290)
25. Tsoularis A, Wallace J. 2002 Analysis of logistic growth models. *Math. Biosci.* **179**, 21–55. (doi:10.1016/s0025-5564(02)00096-2)
26. Simpson MJ, Browning AP, Warne DJ, Maclarens OJ, Baker RE. 2022 Parameter identifiability and model selection for sigmoid population growth models. *J. Theor. Biol.* **535**, 110998. (doi:10.1016/j.jtbi.2021.110998)
27. Canosa J. 1973 On a nonlinear diffusion equation describing population growth. *IBM J. Res. Dev.* **17**, 307–313. (doi:10.1147/rd.174.0307)
28. Fife PC, McLeod JB. 1977 The approach of solutions of nonlinear diffusion equations to travelling front solutions. *Arch. Rational Mech. Anal.* **65**, 335–361. (doi:10.1007/BF00250432)
29. Ablowitz MJ, Zeppetella A. 1979 Explicit solutions of Fisher's equation for a special wave speed. *Bull. Math. Biol.* **41**, 835–840. (doi:10.1016/S0092-8240(79)80020-8)
30. Aronson DG. 1980 Density-dependent interaction–diffusion systems. In *Dynamics and Modelling of reactive systems*, pp. 161–176. New York, NY: Elsevier.
31. Bramson M, Calderoni P, De Masi A, Ferrari P, Lebowitz J, Schonmann RH. 1986 Microscopic selection principle for a diffusion–reaction equation. *J. Stat. Phys.* **45**, 905–920. (doi:10.1007/BF01020581)
32. Vansaarloo W. 2003 Front propagation into unstable states. *Phys. Rep.* **386**, 29–222. (doi:10.1016/j.physrep.2003.08.001)
33. Berestycki J, Brunet É, Derrida B. 2018 Exact solution and precise asymptotics of a Fisher–KPP type front. *J. Phys. A: Math. Theor.* **51**, 035204. (doi:10.1088/1751-8121/aa899f)
34. Berestycki J, Brunet É, Derrida B. 2018 A new approach to computing the asymptotics of the position of Fisher–KPP fronts. *Europhys Lett* **122**, 10001. (doi:10.1209/0295-5075/122/10001)
35. McCue SW, El-Hachem M, Simpson MJ. 2021 Exact sharp-fronted travelling waves of the Fisher–KPP equation. *Appl. Math. Lett.* **114**, 106918. (doi:10.1016/j.aml.2020.106918)
36. Simpson MJ, Treloar KK, Binder BJ, Haridas P, Manton KJ, Leavesley DI, McElwain DLS, Baker RE. 2013 Quantifying the roles of cell motility and cell proliferation in a circular barrier assay. *J. R. Soc. Interface* **10**, 20130007. (doi:10.1098/rsif.2013.0007)
37. Pattle RE. 1959 Diffusion from an instantaneous point source with a concentration-dependent coefficient. *Q. J. Mechanics Appl. Math.* **12**, 407–409. (doi:10.1093/qjmam/12.4.407)

38. Harris S. 2004 Fisher equation with density-dependent diffusion: special solutions. *J. Phys. A: Math. Gen.* **37**, 6267–6268. (doi:10.1088/0305-4470/37/24/005)
39. Vazquez JL. 2006 *The porous medium equation: mathematical theory*. Oxford, UK: Oxford University Press. (doi:10.1093/acprof:oso/9780198569039.001.0001)
40. McCue SW, Jin W, Moroney TJ, Lo KY, Chou SE, Simpson MJ. 2019 Hole-closing model reveals exponents for nonlinear degenerate diffusivity functions in cell biology. *Physica D: Nonlinear Phenomena* **398**, 130–140. (doi:10.1016/j.physd.2019.06.005)
41. Sánchez-Garduño F, Maini PK. 1994 Existence and uniqueness of a sharp travelling wave in degenerate non-linear diffusion Fisher-KPP equations. *J. Math. Biol.* **33**, 163–192. (doi:10.1007/BF00160178)
42. Witelski TP. 1995 Merging traveling waves for the porous-Fisher's equation. *Appl. Math. Lett.* **8**, 57–62. (doi:10.1016/0893-9659(95)00047-T)
43. Witelski TP. 1997 Segregation and mixing in degenerate diffusion in population dynamics. *J. Math. Biol.* **35**, 695–712. (doi:10.1007/s002850050072)
44. Sherratt JA, Marchant BP. 1996 Non-sharp travelling wave fronts in the Fisher equation with degenerate nonlinear diffusion. *Appl. Math. Lett.* **9**, 33–38. (doi:10.1016/0893-9659(96)00069-9)
45. Crank J. 1987 *Free and moving boundary problems*. Oxford, UK: Oxford University Press.
46. Gupta SC. 2017 *The classical Stefan problem. basic concepts, modelling and analysis with quasi-analytical solutions and methods*, 2nd edn. Amsterdam, the Netherlands: Elsevier.
47. Du Y, Lin Z. 2010 Spreading-vanishing dichotomy in the diffusive logistic model with a free boundary. *SIAM J. Math. Anal.* **42**, 377–405. (doi:10.1137/090771089)
48. Du Y, Guo Z. 2011 Spreading-vanishing dichotomy in a diffusive logistic model with a free boundary, II. *J. Differ. Equ.* **250**, 4336–4366. (doi:10.1016/j.jde.2011.02.011)
49. El-Hachem M, McCue SW, Jin W, Du Y, Simpson MJ. 2019 Revisiting the Fisher-Kolmogorov-Petrovsky-Piskunov equation to interpret the spreading-extinction dichotomy. *Proc. R. Soc. A* **475**, 20190378. (doi:10.1098/rspa.2019.0378)
50. El-Hachem M, McCue SW, Simpson MJ. 2021 Invading and receding sharp-fronted travelling waves. *Bull. Math. Biol.* **83**, 35. (doi:10.1007/s11538-021-00862-y)
51. El-Hachem M, McCue SW, Simpson MJ. 2022 Non-vanishing sharp-fronted travelling wave solutions of the Fisher-Kolmogorov model. *Math. Med. Biol.* **39**, 226–250. (doi:10.1093/imammb/dqac004)
52. Bui TTH, van Heijster P, Marangell R. 2024 Stability of asymptotic waves in the Fisher-Stefan equation. *arXiv: 2402.10361.SSRN*. (doi:10.2139/ssrn.4806236). See <https://arxiv.org/abs/2402.10361>.
53. Fadai NT, Simpson MJ. 2020 New travelling wave solutions for the porous-Fisher model with a moving boundary. *J. Phys. A: Math. Theor.* **53**, 095601. (doi:10.1088/1751-8121/ab6d3c)
54. Kreyszig E. 2006 *Advanced engineering mathematics*. New York, NY: Wiley.
55. Morton KW, Mayers DF. 2011 *Numerical solution of partial differential equations*. Cambridge, UK: Cambridge University Press.
56. Rackauckas C, Nie Q. 2017 DifferentialEquations.Jl - a performant and feature-rich ecosystem for solving differential equations in Julia. *J. Open Res. Softw.* **5**, 15. (doi:10.5334/jors.151)
57. Tsitouras Ch. 2011 Runge–Kutta pairs of order 5(4) satisfying only the first column simplifying assumption. *Comput. Math. Appl.* **62**, 770–775. (doi:10.1016/j.camwa.2011.06.002)
58. Simpson MJ, Landman KA, Clement TP. 2005 Assessment of a non-traditional operator split algorithm for simulation of reactive transport. *Math. Comput. Simul.* **70**, 44–60. (doi:10.1016/j.matcom.2005.03.019)
59. Larson DA. 1978 Transient bounds and time-asymptotic behavior of solutions to nonlinear equations of Fisher type. *SIAM J. Appl. Math.* **34**, 93–104. (doi:10.1137/0134008)
60. Murray JD. 1984 *Asymptotic analysis*. New York, NY: Springer. See <http://link.springer.com/10.1007/978-1-4612-1122-8>.
61. Witelski TP. 1994 An asymptotic solution for traveling waves of a nonlinear-diffusion Fisher's equation. *J. Math. Biol.* **33**, 1–16. (doi:10.1007/BF00160171)
62. McCue SW, El-Hachem M, Simpson MJ. 2022 Traveling waves, blow-up and extinction in the Fisher-Stefan model. *Stud. Appl. Math.* **148**, 964–986. (doi:10.1111/sapm.12465)

63. Painter KJ, Sherratt JA. 2003 Modelling the movement of interacting cell populations. *J. Theor. Biol.* **225**, 327–339. (doi:10.1016/s0022-5193(03)00258-3)
64. Landman KA, Pettet GJ. 1998 Modelling the action of proteinase and inhibitor in tissue invasion. *Math. Biosci.* **154**, 23–37. (doi:10.1016/s0025-5564(98)10038-x)
65. Simpson M. 2024 Julia codes for: Fisher-KPP-type models of biological invasion: Open source computational tools to support key concepts and analysis. Github. See <https://github.com/ProfMJSimpson/PDEInvasion>.